Large-Scale Heat and Moisture Budgets over the ASTEX Region

PAUL E. CIESIELSKI, WAYNE H. SCHUBERT, AND RICHARD H. JOHNSON

Department of Atmospheric Science, Colorado State University, Fort Collins, Colorado

(Manuscript received 9 June 1998, in final form 10 November 1998)

ABSTRACT

Rawinsonde data collected from the Atlantic Stratocumulus Transition Experiment (ASTEX) were used to investigate the mean and temporal characteristics of large-scale heat and moisture budgets for a 2-week period in June 1992. During this period a large apparent heat sink and an apparent moisture source were observed near inversion base. Analyses from other budget studies show that similar convective signatures occur in a wide variety of regimes when trade wind–type inversions are present. In the lowest kilometer the vertical eddy flux of moist static energy over the ASTEX domain (centered at 33°N with an average sea surface temperature of 19.4°C) is about 60% of that observed in the undisturbed trade wind regime of BOMEX (centered at 15°N with an average sea surface temperature of 28.1°C).

The apparent heat source, apparent moisture sink, and convective flux of moist static energy over ASTEX were strongly modulated on a synoptic timescale by the passage of fronts and by fluctuations in the subsidence rate associated with changes in the strength and position of the subtropical high. The influence of midlatitude disturbances on convection over ASTEX further distinguishes this region from the trade wind and tropical regimes. Daily budgets are examined for three different convective regimes during ASTEX to determine the mechanisms contributing to the large synoptic variability over this region.

1. Introduction

Understanding the processes that control marine stratus clouds is a crucial step toward accurate simulation of our global climate. Marine stratocumulus, which typically cover 12%–15% of the earth's surface (Randall et al. 1985), in combination with trade cumulus, act as giant humidifiers of the Tropics, supplying much of the energy needed to fuel the Hadley circulation. In addition, satellite and modeling studies have demonstrated the important role of low-level marine stratus clouds as modulators of the earth's radiation budget. While these clouds increase the albedo compared to the underlying ocean, they have little effect on the longwave radiation emitted to space. Satellite analyses have shown that during summer these clouds have a local net cloud radiative forcing of -100 W m^{-2} (Klein and Hartmann 1993) and contribute about -15 W m^{-2} to the global cloud forcing on an annual basis (Hartmann et al. 1992). Emphasizing their importance in climate change, Randall et al. (1984) note that a 4% increase in the global coverage of low-level stratus clouds could actually offset the 2–3 K predicted rise in the global temperature due to a doubling of carbon dioxide.

Because of the importance of stratocumulus and trade cumulus clouds to global climate, several field programs have been designed to study these cloud regimes. In 1969 two field programs were designed to study disturbed and undisturbed conditions in the trade wind regime: the Atlantic Trade Wind Experiment (ATEX) and the Barbados Oceanographic and Meteorological Experiment (BOMEX). Mass and energy transports during ATEX were reported by Augstein et al. (1973, 1974), while Holland and Rasmusson (1973), Nitta and Esbensen (1974, hereafter referred to as NE74), Nitta (1975), and Betts (1975) studied heat and moisture budgets from selected periods of BOMEX. Within the past decade two field programs were conducted to study stratus-type regimes. The first of these, the First International Satellite Cloud Climatology Project Regional Experiment (FIRE), was held in June–July 1987 off the California coast, a region dominated by low, solid stratocumulus clouds during the summer months. The background and goals of FIRE are summarized in Randall et al. (1984), while an extensive overview of key FIRE findings is given by Randall et al. (1996). The next field program, the Atlantic Stratocumulus Transition Experiment (ASTEX), was conducted from 1–28 June 1992 in the subtropical North Atlantic in the area of the Azores and Madeira Islands (Fig. 1). During boreal summer this region is characterized by a 1–2 km deep marine boundary layer (MBL) capped by an inversion of 2–4 K with a variety of cloud conditions including solid

Corresponding author address: Paul E. Ciesielski, Department of Atmospheric Science, Colorado State University, Fort Collins, CO 80523.
E-mail: paulc@tornado.atmos.colostate.edu

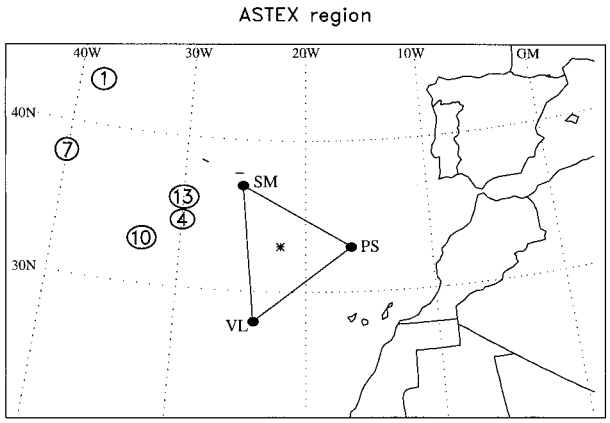

FIG. 1. ASTEX sounding array from 1–15 June 1992. Circled numbers correspond to dates in June 1992 indicating the surface location of the center of the Azores high. The asterisk near the center of the ASTEX triangle shows the position of the buoy described in the text.

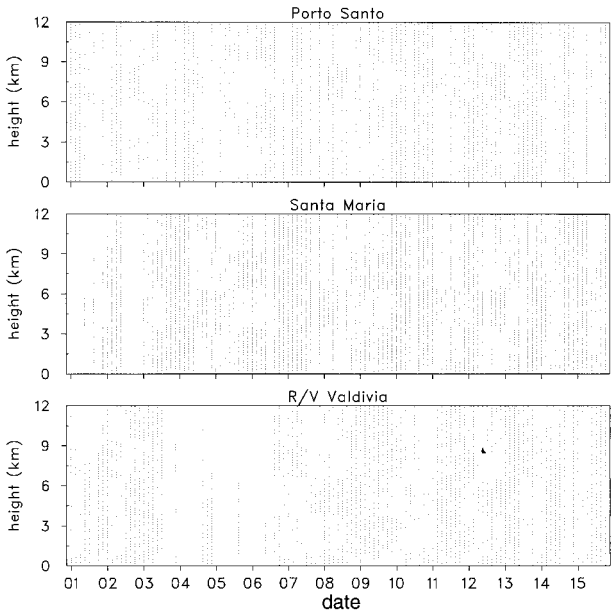

FIG. 2. Visual inventory of sonde data at Porto Santo (top), Santa Maria (middle), and R/V *Valdivia* (bottom) for the period 1–15 June 1992. Each dot depicts the time and altitude of a measurement.

stratocumulus decks, clusters of cumuli penetrating into patchy stratocumulus, broken trade cumulus, and clear skies. The primary goal of ASTEX was to study the processes responsible for the transition from stratocumulus to cumulus regimes. An overview of ASTEX and some early results are given in Albrecht et al. (1995).

The main purpose of this paper is to document the mean properties and synoptic variability of heat and moisture budgets of a stratocumulus transition regime for a 2-week period (1–15 June 1992) during ASTEX and to compare these budgets with those obtained from other regions. In section 2 we describe the data sources for this study and present a brief overview of the synoptic conditions over the ASTEX region for the period in question. Our budget analysis methods are detailed in section 3. Computation of the vertical eddy flux of moist static energy requires radiative divergence profiles. In section 4 we examine the procedure for obtaining these radiation profiles. This is followed by a description of the ASTEX mean budgets and their temporal variability in section 5. Because of the synoptic variability over the ASTEX region, we present (in section 6) daily budgets corresponding to three different convective regimes within the ASTEX region: cumulus penetrating into a stratus deck, intense convective fluxes associated with a frontal passage, and solid stratocumulus. To help us understand the relationship between large-scale budgets and convection, we intercompare sounding, ceilometer, and cloud radar data at Porto Santo for these three convective regimes. Section 7 presents our conclusions. In a forthcoming paper, we describe the diurnal variability of large-scale divergence and vertical motion over the ASTEX region.

2. Data and synoptic overview

a. Data sources

During the 2-week period from 1200 UTC 1 June through 0900 UTC 15 June 1992 the research vessel *Valdivia* (*VL*) was stationed at 28.0°N, 24.0°W. This site, along with the island stations of Porto Santo (PS; 33.1°N, 16.4°W) and Santa Maria (SM; 37.0°N, 25.2°W), define the vertices of the triangle shown in Fig. 1. At these sites high vertical resolution soundings of the atmosphere were taken typically at 3-h intervals. A visual inventory of the sonde data at these sites is shown in Fig. 2. We note from this record that, except for the 4–6 June period at *VL*, data gaps were generally limited to a single missing sonde launch. The sonde data, originally at 5-s (~25 m) intervals, were, for convenience, interpolated from the sea level to the top of the sonde at 25-m intervals. Sea level pressure was computed by integrating the hydrostatic equation downward from the sounding launch height (15, 97, and 50 m, at *VL*, PS, and SM, respectively) by assuming that the density of the underlying layer was a constant equal to the density at launch height. Likewise, values of other variables in the underlying layer were set equal to the launch-height values. The reason for extrapolating data below launch height will become obvious in the next section. Each sounding was then visually inspected and obviously bad data were discarded. Data gaps, as depicted in Fig. 2, were filled in by linearly interpolating the data in time. To reduce high-frequency noise in the wind data, we applied an 11-point filter to the wind components as a function of height with weights $(-1, -5, -5, 20, 70, 98, 70, 20, -5, -5, -1)/256$. This filter effectively damps oscillations on a vertical scale of 125 m and shorter. While the sondes typically recorded data up to at least 12.5 km (about 200 hPa), as shown in Fig. 2, the upper-level winds were frequently

of questionable quality. This is not a problem for the present study, in that its focus is on the trade wind boundary layer, which is typically less than 2 km deep over the ASTEX region. Thus, to avoid the questionable upper-level winds, our vertical motion and budget computations were only carried out up to 600 hPa (~4.5 km). As a boundary condition on vertical motion at this level, we used the European Centre for Medium-Range Weather Forecasts (ECMWF) initialized vertical velocity as described below.

A special set of ECMWF analysis products prepared for the ASTEX period is available at selected pressure levels on a latitude–longitude grid with a horizontal resolution of 1.25° and at 0000, 0600, 1200, and 1800 UTC. By incorporating routine observations from the global network, as well as about 650 supplemental soundings from the normally data-sparse ASTEX region, the large-scale vertical motion field at 600 hPa should be adequately represented in the initialized ECMWF analyses. Because the initialized ω is frequently noisy, we used a 6-h-averaged ω (computed from hourly values) as suggested by Bretherton et al. (1995a). This smoothed omega field at 600 hPa was then averaged over the ASTEX triangle, linearly interpolated in time, and converted to a vertical height velocity using the approximation $w \approx -\omega/(g\rho)$. This provided us 3-hourly values of vertical motion that were used as the top boundary condition in the vertical motion computation. Also from ECMWF's special products for this period we used their analyses of surface fluxes and sea surface temperature (SST). The ASTEX triangle mean SST for 1–15 June 1992 computed from ECMWF's analysis was 19.4°C.

In this study large-scale cloudiness information was obtained from a special cloud classification dataset created for ASTEX by the French Meteorological Office/Centre de Meteorologie Spatiale (CMS). This dataset, which contains hourly estimates of various cloud types at a spatial resolution of 0.08°, is based on the work of Bellec et al. (1992) using METEOSAT data. Utilizing cluster techniques developed by Séze and Desbois (1987), their algorithm partitions the data into classes representative of the following cloud types: thin and thick cirrus, low-level stratus and cumulus, midlevel clouds, and cloud edges. Comparison of their automated scheme to subjective nephanalyses shows an overall good validation, the exception being with nighttime images in which it is difficult to distinguish between the surface and low stratiform clouds.

Cloud properties over the ASTEX domain were deduced using the sounding data described above in conjunction with ceilometer data. In addition, microwave radiometer and cloud radar data were available at PS. Cloud-base information was compiled from the ceilometers with 60-s sampling at PS (1–28 June) and with 30-s sampling at SM (4–23 June) and *VL* (5–15 June) The vertical resolution of the ceilometer data was approximately 8 m. For information regarding the processing of the laser ceilometer data, one should refer to Klett (1981, 1986). Microwave radiometer data were used to retrieve estimates of liquid water path (Hogg et al. 1983; Cahalan and Silberstein 1995) at PS (1–28 June). Also during this same period at PS the National Oceanic and Atmospheric Administration (NOAA) Environmental Technology Lab (ETL) operated a K_α-band (8.7-mm wavelength) radar. Unlike conventional weather radar, which detect primarily cloud particles large enough to be falling from clouds, the K_α-band radar detects airborne cloud particles, or in effect it detects the cloud itself and any precipitation that may be falling out. This cloud radar samples at a vertical resolution of 37.5 m up to 12.3 km so that, as noted by Martner and Kropfli (1993), it produces very detailed images of cloud location and structure, even for multiple cloud decks. For the purposes of this study, we show only ETL's determination (based on radar reflectivity data) of the highest cloud top in the lowest 3 km.

As part of the Subduction Experiment, surface measurements were made at five buoys over the eastern subtropical North Atlantic between June 1991 and June 1993 (Brink et al. 1995). Of particular interest to this study are the measurements made at a buoy located near the center of the ASTEX triangle (33°N, 22°W) as shown in Fig. 1. During the ASTEX period this buoy carried a Vector Averaging Wind Recorder (Weller et al. 1990) instrument system that measured barometric pressure, wind speed and direction, air temperature, sea temperature, relative humidity, and incoming shortwave (SW) and longwave (LW) radiation. From these surface measurements, Moyer and Weller (1997) computed various flux quantities, including sensible heat, latent heat, net shortwave radiation, and net longwave radiation. Table 1 lists the average of these fluxes for the period of interest in this study along with their annual means and a measure of the uncertainty due to instrumental bias. The 2-week mean buoy observations listed in Table 1 were extracted from the time series plots in Fig. 4 of Moyer and Weller (1997). Comparison of these fluxes with estimates from ECMWF analyses and our budgets will be discussed later in this paper.

b. Synoptic overview

To place the budget analyses within the context of the large-scale flow patterns, we provide here a synoptic overview of the ASTEX region for the 1–15 June period. Based on the CMS cloud classification dataset, the average low cloud amount for this period over the ASTEX triangle was 46%. This value compares favorably with that deduced from polar orbiter retrievals for the period 1–23 June, which found total cloudiness over the ASTEX triangle (see Fig. 3 of Bretherton et al. 1995b) to vary from 40%–70% at 0930 UTC [0830 Local Standard Time (LST)] to 35%–50% at 1600 UTC (1500 LST). Figure 3 shows a time series of fractional cloudiness due to low clouds and cirrus derived from the CMS

TABLE 1. Surface fluxes (W m^{-2}) into the atmosphere from ECMWF analyses at 32.5°N, 22.5°W (gridpoint closest to buoy site), computed as a mean over the ASTEX triangle using NCAR's community radiation model (NCRM) and Q_1 and Q_2 budgets, and from buoy observations at 33°N, 22°W. The values listed in columns 2–4 represent 2-week averages for the period 1200 UTC 1 June–0900 UTC 15 June 1992. The last column lists the annual average buoy values and the uncertainties due to instrumental bias.

	The 2-week average			Annual average/uncertainty
Surface flux	ECMWF	NCRM/budgets	Buoy	Buoy
Net shortwave (SW_{net})	−325	−281	−280	−192 ± 7
Net longwave (LW_{net})	84	58	65	66 ± 20
Sensible heat (S_0)	12	11	9	9 ± 3
Latent heat (LE_0)	105	114	91	99 ± 24
Sensible + latent ($S_0 + LE_0$)	117	125	100	108 ± 27
Total heat	−124	−98	−115	−18 ± 54

analyses over the ASTEX triangle. Although cirrus clouds obscure the satellite's view of lower clouds and result in an underestimation of the fractional cloudiness due to low clouds, cirrus clouds were absent during most of the 1–15 June period.

The spatial distribution of total cloudiness shows a general north to south decrease across the ASTEX region (see Fig. 3 of Bretherton et al. 1995b). Ceilometer and CMS satellite–based estimates of low cloud amount at the vertices of the ASTEX triangle corroborate this general pattern despite different viewing angles, spatial volumes, and averaging periods. For example, ceilometer estimates of low cloudiness given by Bretherton et al. (1995b) are 68% at SM (4–23 June), 52% at PS (1–25 June), and 40% at *VL* (6–15 June). For the 1–15 June period, CMS estimates of low cloud amount over a 1° circular area centered at SM, PS, and *VL* are 57%, 45%, and 41%, respectively.

The following discussion of the synoptic conditions over the ASTEX region is based on the daily weather synopsis provided by Bluth and Albrecht (1993). From 1–15 June a strong surface high (maximum pressure about 1030 hPa) was positioned to the north and west of the ASTEX triangle resulting in predominately northerly to northeasterly surface winds varying typically between 5 and 10 m s^{-1} over the region. The mean daily low-level winds at PS, SM, and *VL* are shown in Fig. 4. During this period the average surface wind speed at these sites was 5.2, 4.4, and 7.5 m s^{-1}, respectively, with the high value at the ship being more representative of the wind conditions over the open ocean. The location of the surface high center (as shown in Fig. 1 for selected dates) varied dramatically over the period, affecting the cloudiness and wind conditions. From its position on 1 June the surface high moved southeastward toward the ASTEX region through 4 June. Fractional low cloudiness during this period averaged about 50%. In response to an extratropical cyclone the surface high retrograded westward during 4–7 June. Associated with this cyclone a cold front passed over the northern portions of the ASTEX triangle on 6 June and briefly increased the low cloudiness to nearly 60%. In addition, cyclonic shear associated with the front was observed in the winds between SM and PS on 6 June. Fractional low cloudiness rapidly decreased behind the front from 60% midday on 6 June to 35% late on 7 June. A second stronger cold front moved across the ASTEX region on 8 June briefly increasing the low cloudiness. Behind this front, strong northerlies gusted to near 15 m s^{-1} and a dewpoint drop of 7 K in 4 h was observed at Terceira, which is about 300 km northwest of Santa Maria. After the frontal passage, low cloudiness again decreased to 20% late on 9 June. As the influence of the cyclone lessened

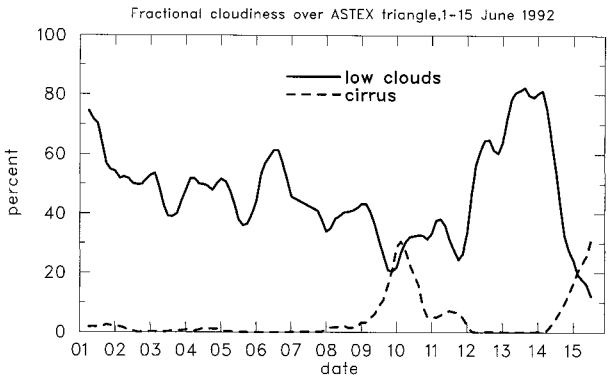

FIG. 3. Fractional cloudiness estimates over the ASTEX triangle for the period 1–15 June 1992 based on the CMS cloud classification dataset.

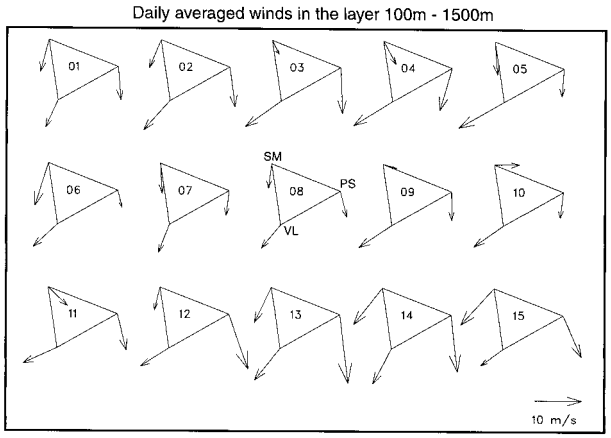

FIG. 4. Daily averaged wind vectors for the 100–1500-m layer for 1–15 June 1992.

during 9–11 June, the surface high again built eastward, reducing the winds and pressure gradient over the ASTEX region. During this period the ridge axis was positioned between SM and *VL*, resulting in strong anticyclonic shear between these sites and a westerly wind component at SM. The surface high continued to strengthen over the region through 13 June, with nearly solid overcast conditions on this date. The strengthening high, in conjunction with a developing low off the Portugal coast, increased the pressure gradient over the region and resulted in strong northeasterly winds of 10–12 m s^{-1}. These strong winds persisted through 15 June when the high began to ridge northward in advance of a cold front. In addition, a cloud-free continental air mass, which had advected from over the Iberian Peninsula, moved over the region dramatically decreasing cloudiness on the low, 15 June.

3. Method of budget analysis

Given the radiosonde array shown in Fig. 1, various methods are available for computing the mass, heat, and moisture budgets. The method chosen here is similar to the line integral technique used by NE74 in their budget analysis of BOMEX. Whereas their analysis was done using pressure-type coordinates, ours is based on the height coordinate and on the anelastic form of the mass continuity equation, that is, $\nabla \cdot \mathbf{v} + \partial(\rho w)/\rho\partial z = 0$, where the air density ρ is assumed to be a known function of z only. First, area-averaged horizontal divergence and relative vorticity over the ASTEX triangle are computed by the line integrals

$$\overline{\nabla \cdot \mathbf{v}} = \frac{1}{A}\oint V_n \, dl, \tag{1}$$

$$\overline{\zeta} = \frac{1}{A}\oint V_t \, dl, \tag{2}$$

where V_t and V_n represent the tangential and outward normal components of the velocity along the periphery of the ASTEX triangle whose area is A. Since spherical distances are used in computations of (1) and (2), this technique automatically includes the effects of convergence of meridians. We wish to use the anelastic continuity equation to compute $\overline{w}(z)$ from observations of $\overline{\nabla \cdot \mathbf{v}}$ by upward integration from $z = 0$, where $\overline{w} = 0$. While use of extrapolated data below the lowest radiosonde observation level could introduce slight errors into the $\overline{w}(z)$ computation, it eliminates the necessity for the special procedures required in the use of pressure coordinates to compute area averages and fluxes when the earth's surface is not a constant pressure surface. To ensure that the vertical motion at the top of the kinematic calculation is equal to the ECMWF value, we define a corrected divergence $\overline{\nabla \cdot \mathbf{v}}^c$ by

$$\rho(z)\overline{\nabla \cdot \mathbf{v}}^c = \rho(z)\overline{\nabla \cdot \mathbf{v}} - \frac{1}{z_T}\left[\rho(z_T)\overline{w}_{\mathrm{EC}}(z_T) + \int_0^{z_T} \rho(z')\overline{\nabla \cdot \mathbf{v}}\, dz'\right], \tag{3}$$

where $\overline{w}_{\mathrm{EC}}(z_T)$ is the ECMWF vertical motion averaged over the ASTEX triangle at height z_T, which is the height of the 600-hPa surface. We then compute the vertical motion by integration of $\overline{\nabla \cdot \mathbf{v}}^c + \partial(\rho\overline{w})/\rho\partial z = 0$ to obtain

$$\rho(z)\overline{w}(z) = -\int_0^z \rho(z')\overline{\nabla \cdot \mathbf{v}}^c \, dz'. \tag{4}$$

By integration of (3) it is easily shown that the corrected divergence satisfies $\rho(z_T)\overline{w}_{\mathrm{EC}}(z_T) = -\int_0^{z_T} \rho(z')\overline{\nabla \cdot \mathbf{v}}^c \, dz'$, so that when (4) is evaluated at $z = z_T$, we obtain $\overline{w}(z_T) = \overline{w}_{\mathrm{EC}}(z_T)$; that is, the kinematically computed vertical velocity $\overline{w}$ equals the ECMWF vertical velocity $\overline{w}_{\mathrm{EC}}$ at $z = z_T$. This adjustment toward ECMWF's values reduces the 2-week mean uncorrected subsidence by 5% at 1 km and 25% at 2 km, or roughly 15% in the layer where the trade inversion typically exists over the ASTEX region.

The apparent heat source Q_1 and the apparent moisture sink Q_2 are defined by

$$Q_1 = c_p\left(\frac{\overline{p}}{p_0}\right)^{\kappa}\left(\frac{\partial\overline{\theta}}{\partial t} + \overline{\nabla \cdot (\mathbf{v}\theta)} + \frac{\partial(\rho\overline{w}\,\overline{\theta})}{\rho\partial z}\right), \tag{5}$$

$$Q_2 = -L\left(\frac{\partial\overline{q}}{\partial t} + \overline{\nabla \cdot (\mathbf{v}q)} + \frac{\partial(\rho\overline{w}\,\overline{q})}{\rho\partial z}\right), \tag{6}$$

where θ is potential temperature, q is the mixing ratio of water vapor, c_p is the specific heat of dry air at constant pressure, L the latent heat of condensation, and $p_0 = 1000$ hPa the constant reference pressure. The line integrals needed in the computations of (1), (2), (5), and (6) assume that the variables $\mathbf{v}$, θ, and q vary linearly along each edge of the triangle. Furthermore, the horizontal flux terms in (5) and (6) are evaluated analytically following Molinari and Skubis (1988). Following Yanai et al. (1973), the apparent heat source Q_1 and the apparent moisture sink Q_2 can be interpreted as

$$Q_1 = Q_R + L(c - e) - \frac{\partial(\rho\overline{w's'})}{\rho\partial z}, \tag{7}$$

$$Q_2 = L(c - e) + L\frac{\partial(\rho\overline{w'q'})}{\rho\partial z}, \tag{8}$$

where Q_R is the radiative heating rate, c the rate of condensation, e the rate of evaporation of cloud water and rainwater, $s = c_pT + gz$ the dry static energy,[1] and

[1] Following Nitta and Esbensen (1974), the apparent heat source is computed in (5) using θ but its interpretion in (7) is in terms of dry static energy (s). The θ form of the apparent heat source equation is slightly more general than the s form, in that the former does not assume hydrostatic balance.

the primes denote deviations from the areal averages. The terms $\rho\overline{w's'}$ and $\rho\overline{w'q'}$ are vertical eddy fluxes of sensible heat and moisture due to dry and moist turbulent and convective motions in the subcloud and cloud layers. The horizontal eddy transport terms $\nabla \cdot (\overline{\mathbf{v}'\theta'})$ and $\nabla \cdot (\overline{\mathbf{v}'q'})$ have been neglected on the premise that the net lateral transports across the ASTEX triangle by cumulus convection are negligible when compared to horizontal transports by large-scale motions.

Subtracting (8) from (7) we obtain

$$Q_1 - Q_2 - Q_R = -\frac{\partial(\rho\overline{w'h'})}{\rho\partial z}, \tag{9}$$

where $h = c_pT + gz + Lq$ is the moist static energy and $\rho\overline{w'h'}$ is the vertical eddy flux of moist static energy. Assuming that $\rho\overline{w'h'}$ vanishes at $z = z_T$, integration of (9) yields

$$\rho\overline{w'h'}(z) = \int_z^{z_T} [Q_1(z') - Q_2(z') - Q_R(z')]\rho(z')\, dz'. \tag{10}$$

In a similar fashion, integrating (7) and (8) from the surface to z_T yields

$$\int_0^{z_T} [Q_1(z) - Q_R(z)]\rho(z)\, dz = LP_0 + S_0, \tag{11}$$

and

$$\int_0^{z_T} Q_2(z)\rho(z)\, dz = L(P_0 - E_0), \tag{12}$$

where $P_0 = \int_0^{z_T} (c - e)\rho(z)\, dz$, $S_0 = \rho_0\overline{(w's')}_0$ and $LE_0 = L\rho_0\overline{(w'q')}_0$ are the amount of precipitation and the supply of sensible and latent heat from the ocean surface, respectively, and the subscript '0' denotes a surface value. From (10), (11), and (12) we note that $\rho_0\overline{(w'h')}_0 = S_0 + LE_0$.

To summarize, we first use the radiosonde wind data to compute the horizontal divergence $\overline{\nabla \cdot \mathbf{v}}(z, t)$ using (1). Then using the ECMWF vertical velocity at $z = z_T$ (≈600 hPa), we compute a corrected horizontal divergence $\overline{\nabla \cdot \mathbf{v}}^c(z, t)$ using (3). The large-scale vertical velocity $\overline{w}(z, t)$ is then kinematically computed using (4). Next, the radiosonde wind, temperature, humidity, and pressure data are used to compute the apparent heat source $Q_1(z, t)$ and the apparent moisture sink $Q_2(z, t)$ from (5) and (6). Finally, the vertical eddy flux of moist static energy $\rho\overline{w'h'}(z, t)$ is computed from (10). This last step requires the radiative heating $Q_R(z, t)$, whose determination is discussed in the next section.

4. Computation of radiative heating profiles

Since observed profiles of $Q_R(z, t)$ are not available for ASTEX, we used the National Center for Atmospheric Research (NCAR) Community Climate Model one-dimensional radiation code (Kiehl et al. 1994) to compute LW and SW radiative profiles at 3-hourly intervals. For clear-sky conditions NCAR's community radiation model (NCRM) requires specification of the sea surface temperature and surface albedo, and the vertical distributions of temperature, water vapor, and ozone. For cloudy conditions, the NCRM also requires specification of the base and top of each cloud layer and the distribution of liquid water within the cloud layer. The sea surface temperature was taken from ECMWF analyses and, for the shortwave calculation, we assumed a surface albedo of 6%, which is reasonable for water surfaces at midlatitudes in summer (Sellers 1965). Radiosonde data from PS, SM, and *VL* provide the required temperature and water vapor profiles. The distribution of ozone was taken from a midlatitude profile of McClatchey et al. (1971). As to the specification of the cloud parameters, we have made the assumption that only one cloud layer exists below the trade inversion. Even with this idealization, the specification of cloud base, cloud top, and the liquid water distribution in the cloud is the most uncertain part of the radiation calculation and is discussed in detail below. Using the radiation model, radiative heating profiles were computed every 3 h with 25-m resolution below 4 km and gradually decreasing resolution above this level.

Let us now discuss some of the details of the radiative calculations. Since our primary goal is to describe the radiative effects of clouds in the vicinity of the trade inversion, we have made the assumption that a single cloud layer exists at or below the trade inversion, with no cloud layers in the upper troposphere. While cloud radar data from PS could be used to specify cloud boundaries at this site, this data source was not available at SM and *VL*. However, use of this information at PS aided the development of a general procedure for defining cloud boundaries at all the sites. Examination of cloud tops detected by radar at PS with coincident soundings (see Fig. 13) shows that the level of the sounding-determined inversion base (I_b) is a good indicator of the radar-determined cloud top (z_{ct}), with z_{ct} generally being within 100 m of I_b. Thus at all the sites cloud top was assumed to be the level of the inversion base found in the soundings. Cloud bases were detected with laser ceilometers at all the sites for at least parts of the 1–15 June 1992 period. For times when ceilometers were operating and clouds were detected, cloud bases (z_{cb}) were determined by averaging ceilometer data over 1 h centered on the sonde launch time. For these same times the lifting condensation level (z_{lcl}) was computed from the sonde data by assuming that the "lifted parcel" had the same θ and q as the sounding average in the lowest 500 m. This allowed us to compute a linear regression relationship between z_{cb} and z_{lcl}. In examining this relationship at SM on 15 June 1992, Miller and Albrecht (1995) found a reasonable agreement between z_{cb} and z_{lcl} when a single cloud layer was present but a rather poor agreement when clouds were multilayered. For times when the ceilometer was in-

operative or no clouds detected, z_{cb} was computed from the regression relationship and the z_{lcl} information from the sonde. If a cloud of thickness less than 150 m was obtained, z_{cb} was reset to be $z_{ct} - 150$ m so that the cloud layer could be adequately resolved by the radiation model with 25-m resolution.

The radiation model also requires specification of the vertical profile of liquid water mixing ratio in the cloud. We assume here that this liquid water mixing ratio profile is given by

$$l(z) = [q(z_{cb}) - q(z)] \exp[-(z - z_{cb})/z_e], \quad (13)$$

where the specified constant, $z_e = 250$ m, is the *e*-folding scale at which the exponential factor decreases with height. Note that, for saturated air, $q(z_{cb}) - q(z)$ is the adiabatic liquid water mixing ratio at height *z*. The justification for the choice $z_e = 250$ m is as follows. The liquid water path (LWP) is proportional to the vertical integral of $l(z)$. Assuming that the air density ρ and water density ρ_w are constants (given as 1.1 and 1000 kg m^{-3}, respectively) and that $q(z_{cb}) - q(z) = \lambda(z - z_{cb})$, we can integrate (13) to obtain

$$LWP = \frac{\rho}{\rho_w} \int_{z_{cb}}^{z_{ct}} l(z)\, dz$$

$$= \frac{\rho}{\rho_w} \lambda z_e^2 \times \left\{1 - \left[1 + \left(\frac{z_{ct} - z_{cb}}{z_e}\right)\right] \exp\left[-\left(\frac{z_{ct} - z_{cb}}{z_e}\right)\right]\right\}, \quad (14)$$

where the liquid water path has the units of water depth. Figure 5 shows plots of the right-hand side of (14) as a function of $z_{ct} - z_{cb}$ for three values of z_e and for $\lambda = [q(z_{cb}) - q(z_{ct})]/(z_{ct} - z_{cb}) = 0.00233/590$ m (based on mean values at PS). Also shown in Fig. 5 are the remote sensing observations of the liquid water path made with the NOAA microwave radiometer (Hogg et al. 1983) installed at PS. Although there is considerable scatter, the choice $z_e = 250$ m provides a good match with the observations over the entire range of cloud thicknesses. With $z_e = 250$ m the PS time average of liquid water path computed from the empirical formula (13) is 0.106 mm, while the time average of the microwave radiometer data is 0.066 mm.

The procedure for computing the ASTEX area average $Q_R(z, t)$, needed in (10), involves the following steps. Compute the radiative heating profile for LW and SW radiation at each of the three sites (PS, SM, and *VL*) for clear $Q_R^{clear}(z, t)$ and cloudy $Q_R^{cloudy}(z, t)$ conditions. The clear-sky cases use the sonde temperature and moisture data, whereas the cloudy cases use the same information but augmented to contain the cloud information described above. Next, the clear-sky radiative heating profiles from each site are averaged to create an ASTEX area mean $\overline{Q}_R^{clear}(z, t)$ and likewise for the cloudy profiles resulting in $\overline{Q}_R^{cloudy}(z, t)$. These mean clear and cloudy profiles are then weighted by the fractional low cloudiness (σ obtained from the CMS analyses shown in Fig. 3) to yield

$$Q_R(z, t) = \sigma(t)\, \overline{Q}_R^{cloudy}(z, t) + [1 - \sigma(t)]\, \overline{Q}_R^{clear}(z, t), \quad (15)$$

which is the ASTEX area average. Equation (15) is evaluated every 3 h so that the time interval for $Q_R(z, t)$ matches the time interval for $Q_1(z, t)$ and $Q_2(z, t)$ in (10).

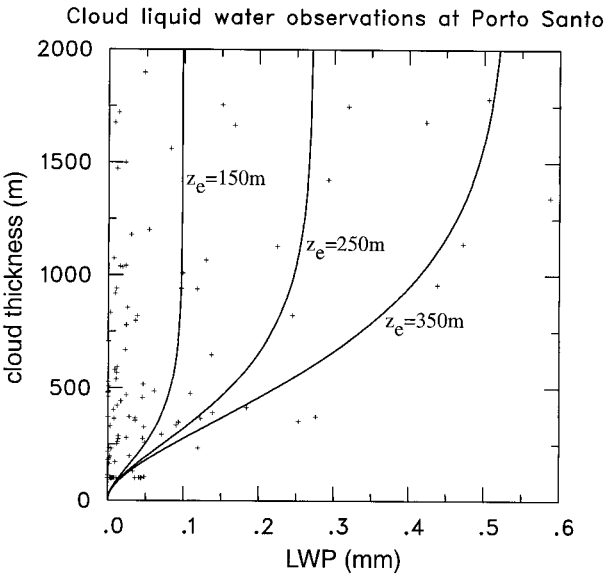

FIG. 5. Observations from 1–15 June at PS of LWP (mm) measured by radiometer cloud thickness. The values of LWP plotted here are 1-h averages centered on the sonde launch time. The solid lines represent the computation of LWP using (14) for different values of z_e.

The accuracy of the radiative computations can be assessed to some degree by comparing the model-generated surface fluxes to those obtained through other means. For this purpose, we list in Table 1 net surface fluxes from ECMWF model analyses, NCRM computations, and buoy observations averaged over the 2-week period in June 1992. Part of the difference between these fluxes may be that the buoy and ECMWF values are point observations while the NCRM values represent a mean over the ASTEX triangle. Of interest here are the small differences in radiative fluxes between the NCRM computations and the buoy observations, which are 1 and 7 W m^{-2}, respectively, for SW_{net} and LW_{net}. These differences are well within the uncertainty limits of the buoy observations shown in Table 1 and much smaller than those between the buoy and the ECMWF fluxes. These comparisons give us confidence that the NCRM results, at least near the surface, are reasonably simulating radiative conditions over the ASTEX region. Furthermore, vertical profiles of longwave radiation produced by the NCRM when clouds are present closely resemble observed profiles taken by the U.K. C-130

aircraft under stratocumulus conditions (Duynkerke et al. 1995) as shown in Fig. 6. A notable difference in these profiles occurs near cloud top where the ''jump'' in net longwave flux is 80 W m^{-2} in the NCRM and 70 W m^{-2} in the observations. While the reasons for this difference are unclear, its effect leads to more cooling (~15%) at cloud top in the model computations compared to the observations. The implications of this difference will be discussed later.

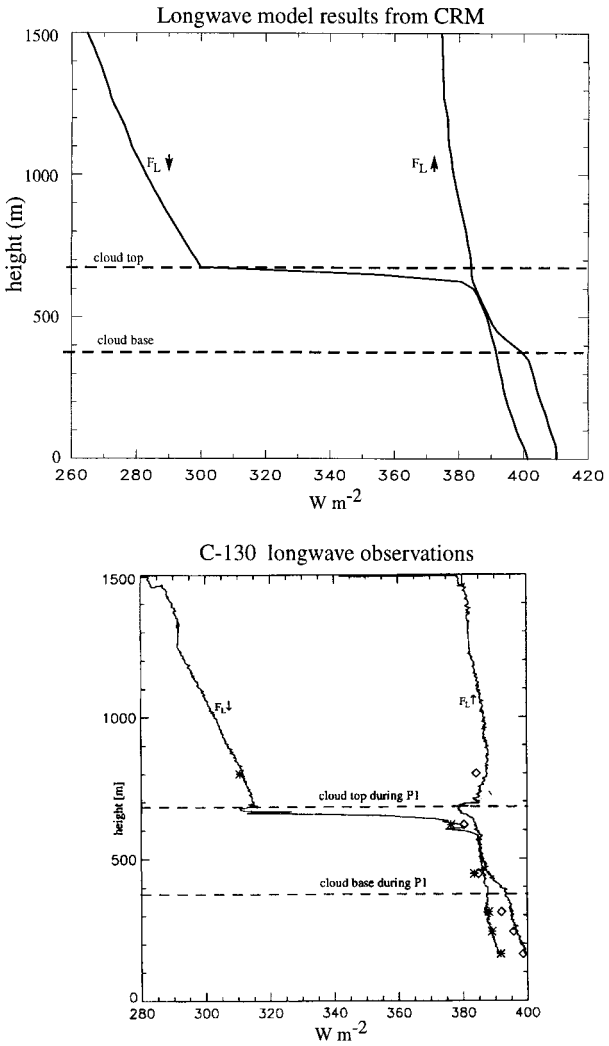

FIG. 6. Comparison of upward ($F_L^{\uparrow}$) and downward ($F_L^{\downarrow}$) longwave fluxes (W m^{-2}) computed with NCAR's community radiation model (top) and the U.K. C-130 aircraft observations taken near SM on 13 June 1992 around 0000 UTC (bottom) (from Duynkerke et al. 1995). The model-computed radiative fluxes were generated using the SM sonde data on 13 June 1992 at 0000 UTC along with cloud information (i.e., top and base location and LWP) given in Duynkerke et al. (1995).

5. Budget means and temporal variability

a. Mean profiles for 1–15 June

Budget and radiative heating computations were carried out for each 3-h observational time from 1200 UTC 1 June to 0900 UTC 15 June. Mean vertical profiles of corrected horizontal divergence, relative vorticity, vertical mass flux,[2] apparent heat source Q_1, apparent moisture sink Q_2, and radiative heating Q_R are shown in Fig. 7. For comparison, similar analyses for a 5-day undisturbed period in the trade wind regime from BOMEX are shown in Fig. 8 (from NE74). During this period over the BOMEX domain, the SST averaged 28.1°C (Delnore 1972) while the surface wind speed averaged 7.5 m s^{-1} (Holland and Rasmusson 1973). Also denoted in Figs. 7 and 8 is the level of trade inversion base (I_b) which for the 1–15 June period over ASTEX averaged 1460 m and for the undisturbed period over BOMEX was at $p^* = 160$ hPa (around 1500 m).[3] For a 6-day period in February 1969 the inversion base over the ATEX region, which was centered near 10°N, 40°W or approximately 2500 km south of the ASTEX region, was also near 1500 m. Despite the fact that these observational studies were conducted in different months, this uniformity in the trade inversion level between these Atlantic regions is consistent with the findings of Schubert et al. (1995) of a quasi-horizontal trade inversion layer in the subtropics.

Focusing on the undisturbed period in BOMEX, we note that in both the ASTEX and BOMEX regions strong divergence occurs at lower levels. For BOMEX the divergence abruptly changes to convergence near inversion base (1.5 km), while for ASTEX this changeover is more gradual, occurring near 2.5 km. While the relative vorticity is negative and nearly constant with height in the trade wind boundary layer over both regions, above this layer anticylonic vorticity decreases in ASTEX and increases in BOMEX. The nearly constant values of divergence and relative vorticity below inversion base and the rapid changes above this level suggest that the horizontal flow below the trade inversion layer is somewhat mixed and at least partially decoupled from the flow above. Augstein et al. (1973) found similar behavior over the ATEX region and noted that the time variations of the horizontal flow increased above the trade inversion. Such flow differences across the inversion layer led some early studies of the trade wind regime (e.g., von Ficker 1936) to erroneously conclude that the strong stability of the trade inversion acts as a lid through which no air moves. In studying the Pacific trade wind regime, Riehl et al. (1951) were among the first to dispel this impermeability notion,

[2] For comparison with previous budget studies we have multiplied our computed mass flux $\rho\overline{w}$ by the constant $-g$, which can be interpreted as the vertical pressure velocity (i.e., $\omega \approx -g\rho\overline{w}$). We have labeled several figures (e.g., Figs. 7, 10, 14) with the term ''omega,'' even though the field actually calculated is $-g\rho\overline{w}$.

[3] In NE74 $p^* = p_{\text{surface}} - p$, such that a negative vertical p^* velocity signifies sinking motion.

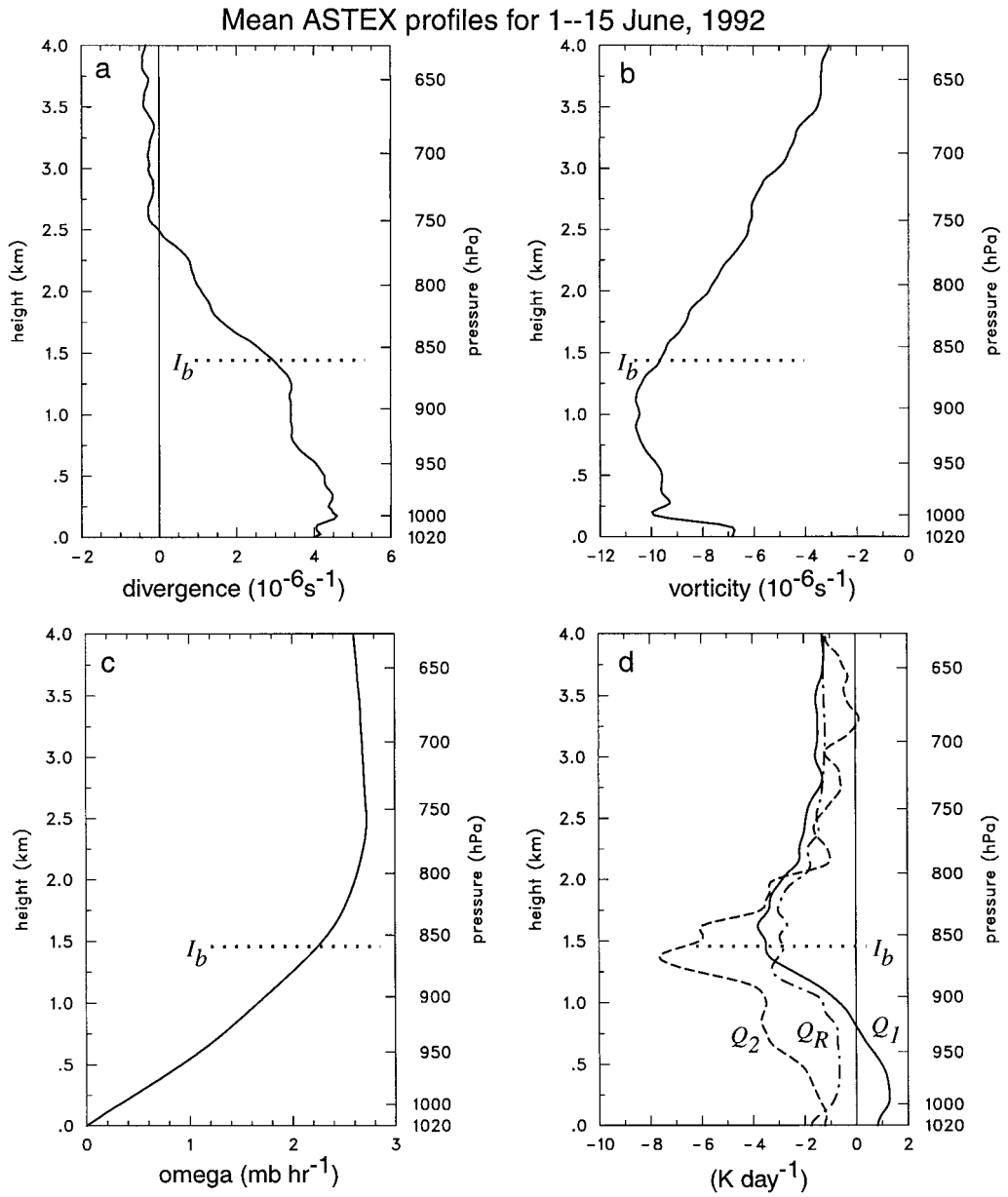

FIG. 7. Mean profiles of (a) divergence, (b) relative vorticity, (c) omega, and (d) apparent heat source Q_1 (solid), apparent moisture sink Q_2 (dashed), and net radiative heating Q_R (dash–dotted) for 1–15 June 1992 over the ASTEX triangle. Dotted line at 1460 m indicates the average level of the inversion base (I_b) for this period.

stating that downward mass transport occurred through the inversion layer. Results from ATEX and BOMEX corroborate Riehl et al.'s findings, showing in fact that subsidence maximizes near the inversion base with rates of 2.6 and 2.0 mb h^{-1}, respectively. The pressure velocity profiles from ASTEX (Fig. 7c) and the BOMEX undisturbed period (Fig. 8c) exhibit sinking motion throughout the entire trade inversion layer with subsidence rates of 2.0 mb h^{-1} at the inversion base for both regions. While subsidence maximizes near this level for BOMEX, the 2.7 mb h^{-1} peak for ASTEX is located somewhat higher, near 2.5 km.

Vertical profiles of Q_1 and Q_2 from ASTEX (Fig. 7d) and BOMEX (Fig. 8d) are similar in many respects. Both regions show a large apparent heat sink and apparent moisture source near the inversion base.[4] Interpreting the BOMEX budgets with a cloud model, Nitta (1975) attributes these features primarily to the cooling and moistening effects of cloud detrainment near the

[4] A Q_2 rate of -10 K day^{-1} is equivalent to a moistening rate of 4 g kg^{-1} day^{-1}.

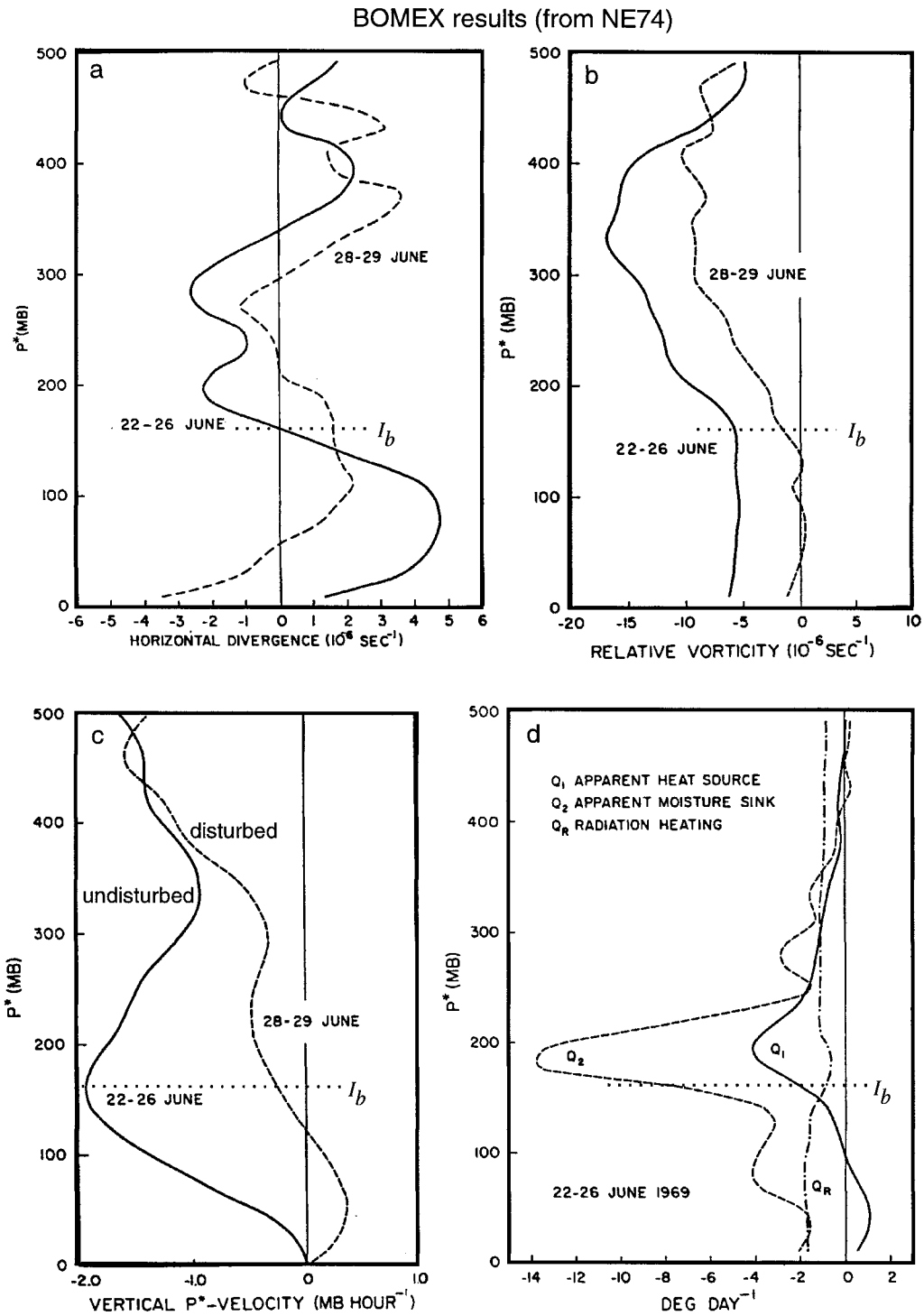

FIG. 8. Mean profiles of (a) divergence, (b) relative vorticity, (c) vertical p^* velocity for disturbed (dashed lines) and undisturbed (solid lines) conditions during BOMEX. Vertical profiles of (d) apparent heat source Q_1 (solid), apparent moisture sink Q_2 (dashed), and radiational heating Q_R (dash–dotted) for a 5-day undisturbed period. These figures were taken from NE74. Dotted line at $p^* = 160$ hPa indicates the average level of the inversion base (I_b) for the undisturbed period.

inversion layer. While the cooling rates peak around −4 K day^{-1} over both regions, moistening rates near the inversion are smaller for ASTEX (−8 K day^{-1} compared to −14 K day^{-1} for BOMEX). While this difference may be due in part to the higher moisture contents over BOMEX, one must also consider that the ASTEX-averaged profiles in Fig. 7 are for a significantly longer period (14 days compared to 5 days for BOMEX). During the 1–15 June period, daily averaged Q_2 rates near I_b for ASTEX varied from slightly positive to −40 K day^{-1} (see time series of Q_2 in Fig. 11 and selected daily means in Fig. 15). The displacement of the moistening peak slightly above the inversion base for BOMEX and slightly below it for ASTEX may reflect stability differences between the two regions. For example, summertime inversion strengths (i.e., the temperature difference between the inversion top and base) over the Caribbean are typically 0.7 K (Gutnick 1958), while the average inversion strength for 1–15 June 1992 over the ASTEX region was 2.8 K. The weaker stability of the trade stable layer over the BOMEX region may allow clouds to penetrate farther into the inversion layer before they detrain their mass and moisture. Above the trade inversion layer, as convective effects diminish, the Q_2 profiles decrease to zero. In contrast, while the Q_1 profile for BOMEX tends to zero, for ASTEX it approaches a cooling rate of −1 to −2 K day^{-1}, consistent with computed radiative cooling rates in this layer. At levels below cloud base, the positive $Q_1 - Q_R$ and negative Q_2 values are due to convergence of vertical eddy fluxes of heat and moisture.

Differences in the mean vertical profiles of Q_R between the ASTEX and BOMEX regions are most pronounced near the inversion layer. For example, the BOMEX profile[5] has a minimum in radiative cooling (−0.5 K day^{-1}) near I_b. In contrast, the ASTEX profile has cooling rates that maximize around −3 K day^{-1} in a broad layer between 1.2 and 1.7 km centered near I_b. As suggested by the divergence in the longwave flux near cloud top in Fig. 6, radiative cooling maximizes at or slightly above cloud top. The flux divergence observed near cloud top in the bottom panel of Fig. 6 translates into a cooling rate of ≈62 K day^{-1} over a 100 m deep layer. The effects of fractional cloudiness and a cloud top that varies both spatially over the ASTEX triangle and temporally over the 2-week period result in the broadness and the reduced magnitude of the mean peak cooling rate observed in Fig. 7d. The fact that the BOMEX Q_R profile is more representative of radiative fluxes under clear-sky conditions suggests that the Q_R differences seen between Figs. 7 and 8 are due largely to a higher fractional cloudiness over the ASTEX region.

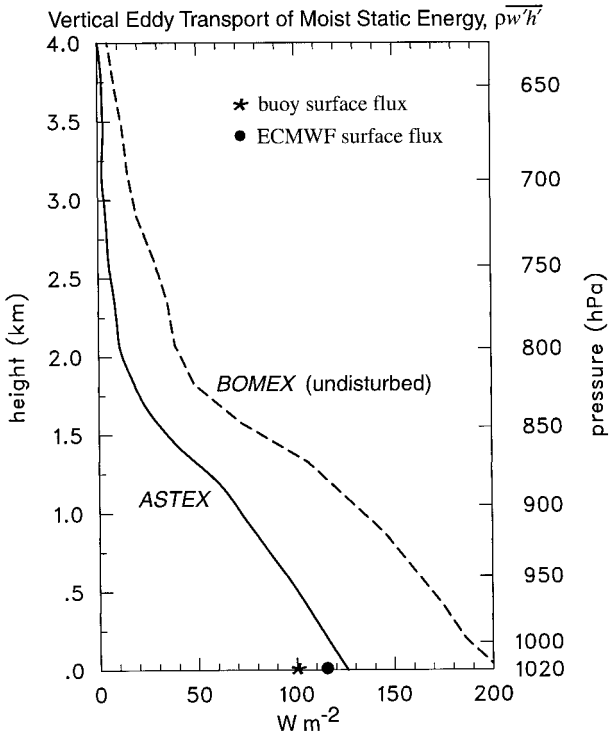

FIG. 9. Mean profiles of vertical eddy flux of moist static energy for 1–15 June 1992 over the ASTEX triangle (solid) and for the undisturbed period over BOMEX (dashed). Also indicated are the mean values of latent plus sensible heat fluxes at the surface for 1–15 June 1992 from buoy observations (denoted with an asterisk) and from ECMWF analyses (denoted with a filled circle).

Figure 9 compares the 2-week mean ASTEX profile of vertical eddy flux of moist static energy to that for the undisturbed period in BOMEX (curve from NE74). The ASTEX profile shown here was computed from (10). With this procedure we find that the ASTEX mean vertical eddy flux decreases from its surface maximum of 125 W m^{-2} almost linearly with height to 1.2 km. At this level the flux decreases more rapidly to about I_b (≈1460 m) and then less rapidly to 2 km where the flux is only 10% of its surface value. Over the lowest kilometer the ASTEX fluxes are approximately 60% of the BOMEX fluxes. At the ocean surface, fluxes are proportional to wind speed and interfacial temperature and moisture gradients. In evaluating the latent heat flux, which over water dominates the sensible heat flux, the moisture gradient is computed as the difference in the saturation mixing ratio at the ocean surface, q^*, and the mixing ratio at some reference level in the boundary layer. While wind speeds observed during BOMEX and ASTEX are roughly the same (6–8 m s^{-1}), the SST difference between these regions (28.1°C in BOMEX vs 19.4°C in ASTEX) results in a q^* that is substantially higher in BOMEX (25 g kg^{-1} vs 15 g kg^{-1} in ASTEX). Despite the moister boundary layers in BOMEX, its

[5] The BOMEX Q_R profile shown by NE74 and reproduced in Fig. 8d comes from a preliminary BOMEX radiation dataset. Averaging the final dataset, computed using sounding data and observed cloud distributions (Cox 1973) from 22–26 June 1969, produces essentially the same Q_R profile as shown in Fig. 8d.

high q^* results in air–sea moisture gradients (and thus surface fluxes) that are nearly twice as large as those in ASTEX.

To assess the accuracy of our budget computations of $\rho\overline{w'h'}$, we also show in Fig. 9 estimates of surface sensible and latent heat flux from ECMWF analyses and that derived from buoy observations.[6] These surface fluxes, individually and their sum, are listed in Table 1. The budget-derived values for sensible and latent heat flux listed here were computed by evaluating the lhs of (11) and (12), respectively, and by specifying LP_0 to correspond to a rainfall rate of 0.16 mm day^{-1}. Since the actual rain rate over ASTEX for this period was not known,[7] this rate was chosen so that the Bowen ratio (S_0/LE_0) would be 0.1, consistent with the ASTEX buoy observations for this 2-week period and with in situ observations from BOMEX (Pond et al. 1971). Although our budget-derived value of $\rho_0\overline{(w'h')}_0$ and ECMWF's estimate are within the uncertainty limits of the buoy data, both appear to be too large. With regard to the ECMWF's excessive flux, Bretherton et al. (1995b) note that a moist bias of 1 g kg^{-1} in ECMWF analyses of the ASTEX surface layer may be a result of a surface latent heat flux that is too large by 10 W m^{-2}. As noted earlier, our radiation model computations produced about 15% more radiative cooling at cloud top than observed, which translates into an additional sensible heat flux at the surface of 5 W m^{-2}. Even by adjusting $\rho_0\overline{(w'h')}_0$ downward by this amount, it appears that our budget estimates of vertical eddy fluxes may be too large by about 20%. Due to the large subsidence rates and vertical gradients of thermodynamical fields in the inversion layer over the ASTEX region, the effects of vertical advection dominate over the other terms in (5) and (6) in determining Q_1 and Q_2 structures. This suggests that the excessive budget-derived fluxes may result from computed subsidence rates (and thus low-level divergences) that are too high. The appendix examines how sampling and interpolation errors may have affected our divergence calculations. Finally, by adjusting the fractional cloud amount (σ) in (15) we find that a 5% increase (decrease) in σ results in a 3 W m^{-2} increase (decrease) of $\rho_0\overline{(w'h')}_0$.

In addition to showing the 2-week-averaged surface fluxes computed from buoy data, Table 1 also lists their annual averages (taken from Table 2 of Moyer and Weller 1997). While the 2-week buoy means of LW_{net} and heat fluxes shown in Table 1 are close to their annual averages, the 2-week means of SW_{net} and total heat flux, being significantly larger than their annual averages, are typical of summer conditions over this region. In the following section we show how the budget-derived fluxes over ASTEX vary during a 2-week time period in June 1992. Over a longer period, Moyer and Weller (1997) show time series of 4-day smoothed heat fluxes from ECMWF analysis and computed from buoy data over ASTEX during 1992. These filtered time series vary from minimum values of a few watts per meter squared during several periods from spring through early summer to maximum values over 400 W m^{-2} in the ECMWF analyses (300 W m^{-2} in the buoy data) during several episodes in late fall.

b. Time series for 1–15 June

Because of the large daily variability in cloudiness and synoptic conditions over the ASTEX region during the 1–15 June period, we now examine the temporal variability of large-scale fields and budgets. Figure 10 shows the time series (15-h running means) of relative vorticity, divergence, and omega for the period of interest. Also indicated in these figures (with a dashed line) is the daily average level of inversion base. While the level of the inversion base varies on a daily basis in response to changes in the large-scale subsidence field, its overall trend through the period is to gradually lower from around 1800 m on 1 June to under 1200 m on 15 June. From the relative vorticity time series we see that the flow over the ASTEX region is strongly anticyclonic below inversion base except for the brief period on 6–8 June when two cold fronts passed through the ASTEX region. Weak convergence was also observed at lower levels during part of this period, while the remainder of the time series was marked by strongly divergent flow below inversion base. The omega time series is dominated by subsidence, with peak rates often located well above the inversion base and a large synoptic variability related to the position of the surface high and the passage of midlatitude systems to the north of the ASTEX triangle. This time series also shows that increased subsidence tends to lower the inversion level, consistent with mixed-layer thermodynamic models of stratocumulus (Lilly 1968).

Figure 11 shows the time series (15-h running means) of Q_1, Q_2, Q_R, and $\rho\overline{w'h'}$ for 1–15 June 1992. The time series of Q_1, Q_2, and Q_R show that the peak rates are generally centered near the inversion base (i.e., near cloud top). Secondary peaks, such as those observed in Q_1 and Q_2 near 2800 m on 2 June and in Q_2 near 800 m on 3 and 4 June, are an indication of multiple cloud and moisture layers. The periods with peak radiative cooling in Fig. 11 occur on 3 June, when the inversion (and cloud top) slope across the ASTEX domain was relatively flat, and on 13 June (middle panel of Fig. 15), when fractional cloud cover was quite high (~80%).

[6] White et al. (1995) also give an observation of a surface sensible plus latent heat flux ($S_0 + LE_0$) over the ASTEX domain. Their estimate of 84 W m^{-2}, which is derived from data taken on R/V *Malcolm Baldridge* during the period 7–28 June 1992, is consistent with buoy observations for this same period.

[7] Summertime climatological values of precipitation rate over the ASTEX region are ~0.5 mm day^{-1} (Dorman and Bourke 1981), which equates to 14.5 W m^{-2}. For the undisturbed period in BOMEX, Holland and Rasmusson (1973) assume a precipitation rate of 0.2 mm day^{-1}.

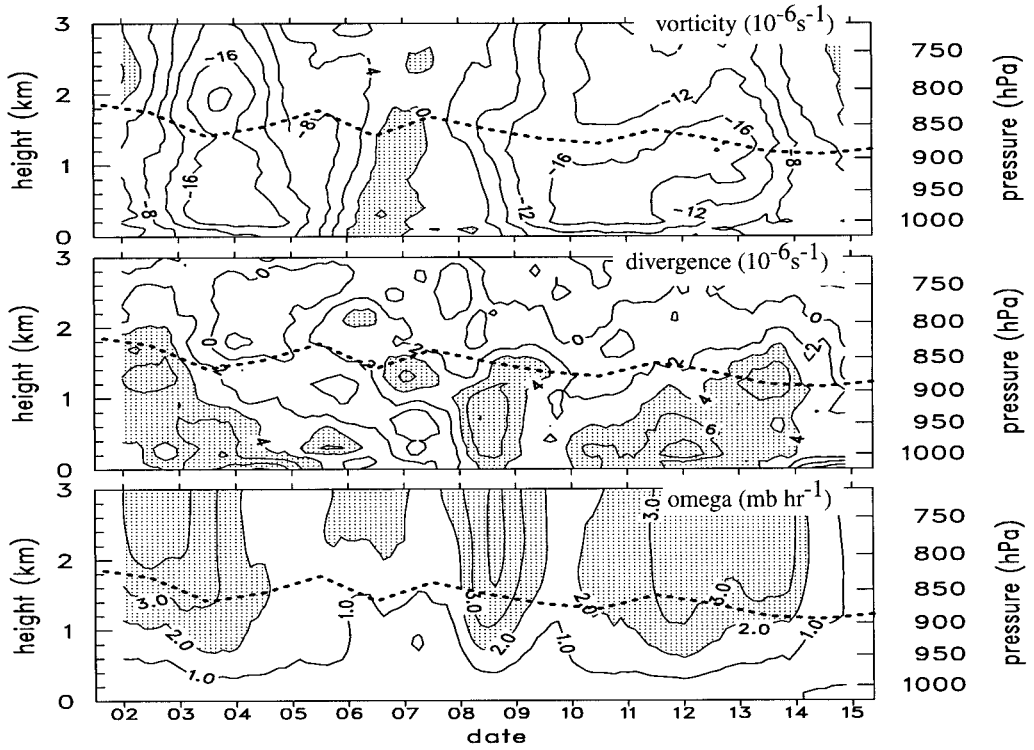

FIG. 10. Time series (15-h running mean) of relative vorticity (positive values shaded with increment 4×10^{-6} s^{-1}), divergence (positive values greater than 4×10^{-6} s^{-1} shaded with increment 2×10^{-6} s^{-1}), and omega (values greater than 2 mb h^{-1} shaded with increment 1 mb h^{-1}) for 1–15 June 1992 over the ASTEX triangle. Dashed lines indicate the daily average level of inversion base.

This is consistent with our previous observation that area-averaged radiative cooling rates near cloud top can be enhanced when spatial variations in the cloud-top level are small and when fractional cloudiness is high. The $\rho\overline{w'h'}$ time series shows that fluxes are generally negligible above 2 km but exhibit rapid change through the inversion layer. The temporal variability of these quantities is strongly modulated on a synoptic timescale by the passage of fronts and fluctuations in the subsidence rate associated with changes in the strength and position of the subtropical high. For example, during this 2-week period the vertical eddy flux varies between zero and two times its mean value (shown in Fig. 9) on a scale of a few days.

To help interpret how the variability of these fields is related to *actual* moistening and changes in low-level cloudiness (Fig. 3), we show in Fig. 12 the time series of omega and perturbation specific humidity averaged from 1 to 2 km (i.e., the layer that contains the trade inversion where Q_1 and Q_2 typically maximize). Whether *apparent* moistening leads to *actual* moistening depends on competing effects, namely, convection, which tends to moisten the inversion layer, and subsidence, which tends to dry it out. For example, on 2 and 3 June subsidence drying dominates over convective moistening such that the inversion-layer moisture decreases by 1 g kg^{-1}. This period contrasts to those on 4–5 June and 10–11 June when convective fluxes dominate over the drying effects of subsidence, thereby moistening the inversion layer by 2 g kg^{-1}. These strong *actual* moistening events precede periods of rapid cloudiness increase (25% on 5 June and 40% on 12 June; see shaded periods in Fig. 12) over the ASTEX domain that coincide with periods of reduced subsidence.

6. Analyses of different convective regimes

As described in the previous sections, the ASTEX region during the 1–15 June period was characterized by widely varying synoptic and cloud conditions. In this section we further investigate this temporal variability by examining the atmospheric conditions associated with three types of convective regimes that occurred during this fortnight period and are common to the ASTEX region. For this purpose we have selected three 24-h periods during which the following conditions predominated: cumulus penetrating into a stratus deck (4 June), intense convective fluxes associated with a frontal passage (8 June), and finally, solid stratocumulus (1000 UTC 13 June to 0900 UTC 14 June). The goal here is to examine these convective regimes with different perspectives: from the large-scale using heat and moisture budgets from which convective effects can be inferred, down to the cloud-scale using various instrument plat-

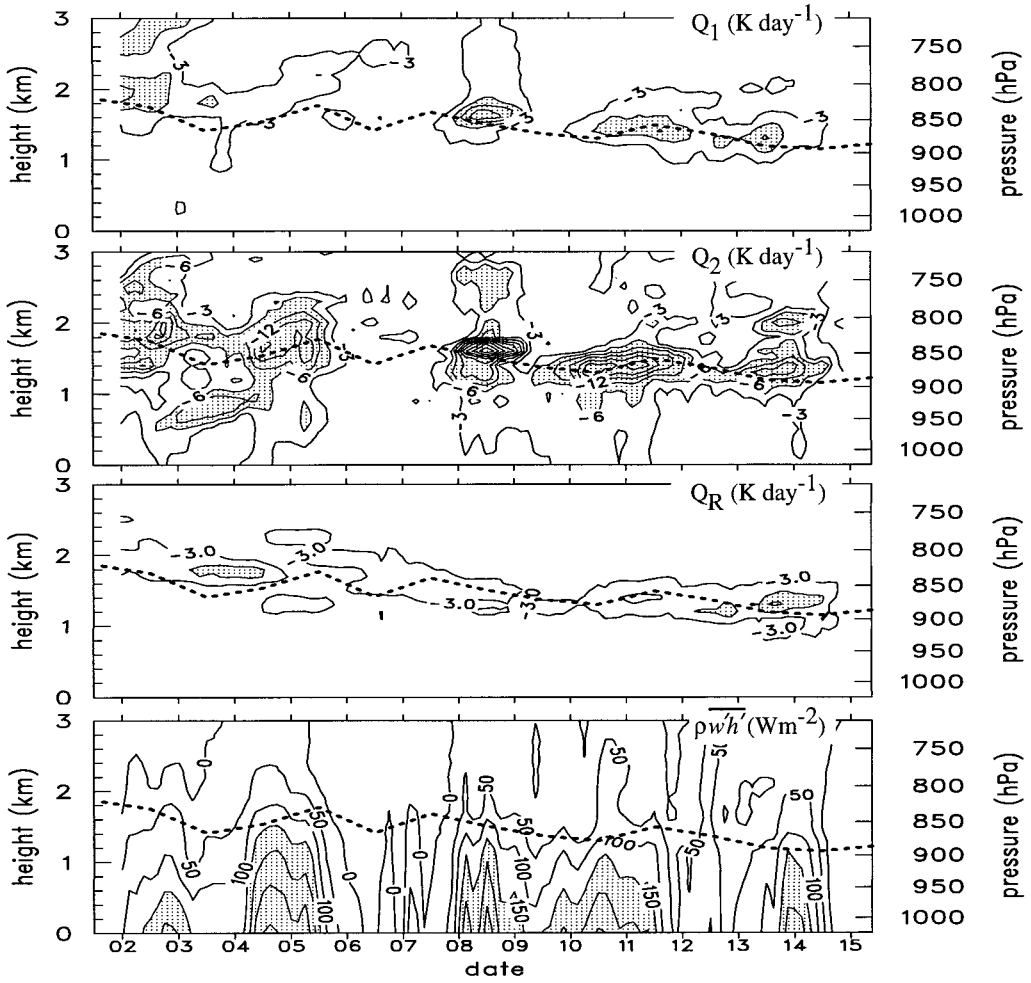

FIG. 11. Time series (15-h running mean) of apparent heat source Q_1, apparent moisture sink Q_2, net radiative heating Q_R (values less than -6 K day^{-1} shaded with increment 3 K day^{-1}), and vertical eddy flux of moist static energy $\rho\overline{w'h'}$ (values greater than 150 W m^{-2} shaded with increment 50 W m^{-2}) for 1–15 June 1992 over the ASTEX triangle. Dashed lines indicate the daily average level of inversion base.

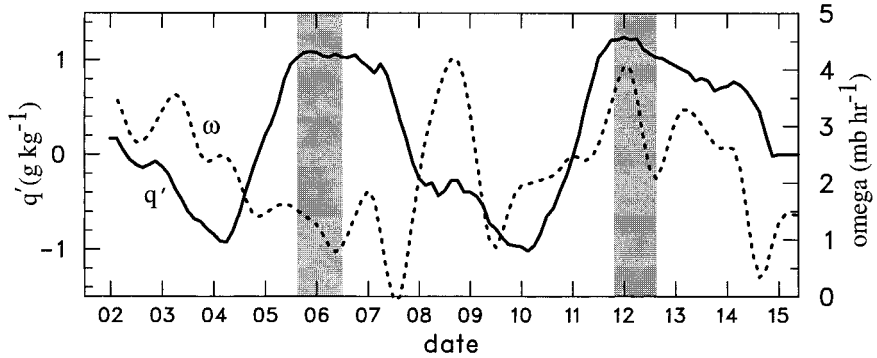

FIG. 12. Time series (15-h running mean) of perturbation specific humidity (solid line) and omega (dashed line) averaged over the 1–2-km layer for 1–15 June 1992 over the ASTEX triangle. Shaded periods on 5–6 June and 11–12 June indicate periods when low-level cloudiness over the ASTEX domain increased by 25% and 40%, respectively.

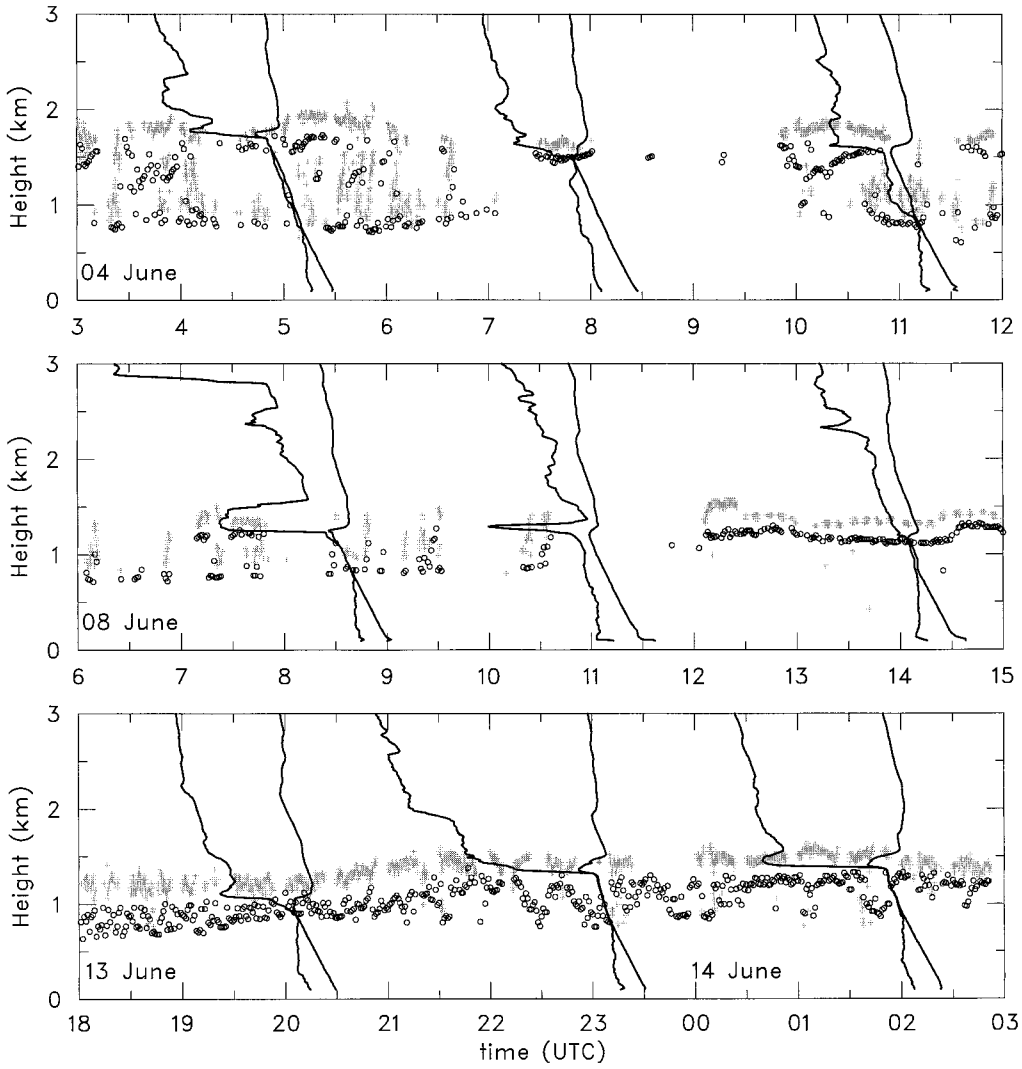

FIG. 13. Data collected at Porto Santo indicating three types of convective regimes: cumulus penetrating into stratus (top: 4 June from 0300 to 1200 UTC) intense convective fluxes associated with a frontal passage (middle: 8 June from 0600 to 1500 UTC), and solid stratocumulus deck (bottom: 13 June at 1800 UTC to 14 June at 0300 UTC). Circles denote cloud base as determined by laser ceilometer, light gray plus signs denote cloud top as determined by cloud radar, pairs of curves represent rawinsonde temperature (right), and dewpoint temperature (left) data aligned on the time axis such that the temperature data at 1.5 km are correctly timed.

forms that detect clouds and their properties directly. Because of the collocation of several such instruments (rawinsonde system, 8.7-mm Doppler cloud radar, and a laser ceilometer that are described in section 2) at PS, we have elected to use the data sources from this site.

Figure 13 shows time series of cloud-top height (inferred by radar) and cloud-base height (inferred by ceilometer) at Porto Santo for a 9-h period from each of the three days of interest. Superimposed on these plots are radiosonde thermodynamic data that are aligned in time such that the temperature curves intersect the 1.5-km level approximately 5 min after sonde launch, assuming a balloon rise rate of 5 m s^{-1}. While cloud Doppler radar also detects cloud base, these estimates are not shown here. Stevens (1994) found that under solid stratocumulus conditions at PS, ceilometer and cloud Doppler radar estimates of cloud-base height agree reasonably well, but less so under mixed cumulus–stratocumulus conditions. He also found good agreement when clouds were optically thick. However, when detecting optically thin clouds, the ceilometer appeared more sensitive to clouds above 1 km (e.g., between 0800 and 1000 UTC on 4 June), while the radar was better at detecting thin clouds below this level. Comparisons of cloud bases from these two instruments is further complicated by the presence of precipitation. For example, in Fig. 16 from Albrecht et al. (1995), the ceilometer detects a cloud base around 1 km whereas the

cloud radar detects the drizzle falling below this base. Clouds boundaries can also be inferred from saturated layers in the sonde data. These layers, observed in Fig. 13, suggest the presence of clouds at slightly lower elevations than indicated by ceilometer and radar estimates. This disparity is most obvious at cloud top, where at times the temperature and dewpoint curves diverge at least 100 m below the radar's determination of cloud top. Finally, we note that negative departures in temperature and dewpoint that occur just above inversion base after the sonde emerges from a cloud layer (especially obvious on 13 June when a solid stratocumulus deck was present) is likely due to evaporation of moisture that has condensed on the sonde's temperature sensor. This effect only appears in the sonde data at PS, which used a VIZ sonde package, and not at SM and *VL* (cf. Fig. 16), which used Vaisala RS80 thermodynamic packages.

The time series for 4 June (top panel in Fig. 13) suggests the presence of multiple cloud layers at PS. An upper cloud layer, most likely a thin stratocumulus deck, was present between 1.5 and 2.0 km under which a second layer of clouds was periodically observed with bases around 800 m and tops frequently extending into the upper layer. This type of cloud field with cumulus penetrating into stratocumulus was proposed (Bretherton 1992; Wyant et al. 1997) as an important stage in the transition of subtropical stratocumulus into trade cumulus. Fractional low cloudiness over the ASTEX triangle on 4 June was 49.1% (cf. Fig. 3). The time series for 8 June (middle panel in Fig. 13) also shows multiple cloud layers early in the time sequence followed by the presence of a thin stratus sheet. The soundings at PS were generally moist below 3 km on 8 June, except for a shallow layer immediately above inversion base that also moistened through the course of the day. Fractional low cloudiness increased over the ASTEX triangle on 8 June from 35% to 45%. The time series for 13–14 June (bottom panel in Fig. 13) shows a single solid stratocumulus deck. Between 2000 and 2300 UTC the air above the trade inversion dried out while below this level the MBL moistened and deepened about 250 m. Fractional low cloudiness over the ASTEX triangle for this period averaged nearly 80%. This last period occurs near the middle of the first Lagrangian experiment of ASTEX, which lasted from 12 to 14 June. Analysis of this Lagrangian experiment is presented in de Roode and Duynkerke (1996, 1997).

Averaged flow fields and budgets for the three periods of interest are shown in Figs. 14 and 15. Also indicated here is the level of inversion base, which was highest and weakest on 4 June and lowest and strongest for the 13–14 June period. Differences between these daily averaged fields are quite striking. For example, relative vorticity varies between strongly anticyclonic through a deep layer on 4 June to near zero at the surface on 8 June. The divergence profiles, while being positive below inversion base, peak at different levels: near the surface on 4 June, near the middle of the MBL on 8 June, and near inversion base on 13–14 June. The strong vertical gradients of vorticity and divergence in the near-surface layer on 4 June may indicate a decoupled boundary layer during this period. Through analyses of NCAR Electra aircraft data from ASTEX, Wang and Lenschow (1995) showed that the boundary layer is generally decoupled from the near-surface air when penetrating cumulus clouds are present, except in the vicinity of cumulus. This contrasts to the more homogeneous structure of the boundary layer flow field associated with the solid stratocumulus conditions on 13–14 June. Vertical motion differences (bottom panel of Fig. 14) in the trade inversion layer range from weak subsidence on 4 June to strong sinking for the latter two periods. On 4 and 8 June the subsidence field has a peak at the inversion base, similar to that observed in BOMEX (NE74) and in ATEX (Augstein et al. 1973). However, on 13–14 June the peak subsidence is located near 2 km, which is well above the inversion base.

Apparent heat source and apparent moisture sink profiles for these three periods are shown in the top panels of Fig. 15. On 4 June the Q_1 and Q_2 profiles have two cooling and moistening peaks: a main peak near 1.7 km and a secondary peak near 1 km. The lower peak may reflect the effects of small cumuli under a stratocumulus deck. The peak cooling and moistening rates on 4 June are quite similar to those observed by NE74 (cf. Fig. 6) for an undisturbed period in BOMEX. On 8 June the profiles of Q_1 and Q_2 are dominated by enormous apparent moistening and cooling peaks just above inversion base. The daily averages of Q_1 and Q_2 near this level are -20 and -40 K day^{-1}, respectively. Following the frontal passage, which occurred around 0900 UTC at SM and 1800 UTC at PS, enhanced winds coupled with a drier air mass resulted in increased surface and convective fluxes (Fig. 11 and bottom panel of Fig. 15). The Q_1 and Q_2 peaked at 15 UTC with values more than double the daily average. Associated with the frontal passage, subsidence also increased with peak rates of 4 mb h^{-1} near inversion base at 1800 UTC (Fig. 10). Despite the presence of strong subsidence, intense convective fluxes during this period dominated over these drying effects to moisten the dry layer observed at PS (middle panel of Fig. 13) above inversion base at 0900 UTC resulting in a thin stratocumulus sheet by 1500 UTC. Such events of intense convective fluxes associated with midlatitude disturbances distinguish the ASTEX region from that of trade wind regimes in which convection associated with tropical disturbances results in little, if any, apparent cooling and moistening effects below 700 hPa (see Fig. 8 of NE74). During the 13–14 June period we again observe two prominent Q_1/Q_2 peaks. The primary Q_1/Q_2 peaks occur slightly above the inversion base with apparent cooling and moistening rates of 7.5 K day^{-1} and 8 g kg^{-1} day^{-1}, respectively; the secondary peaks occur near 2 km. Since the PS data in the bottom panel of Fig. 13 show no evidence of a

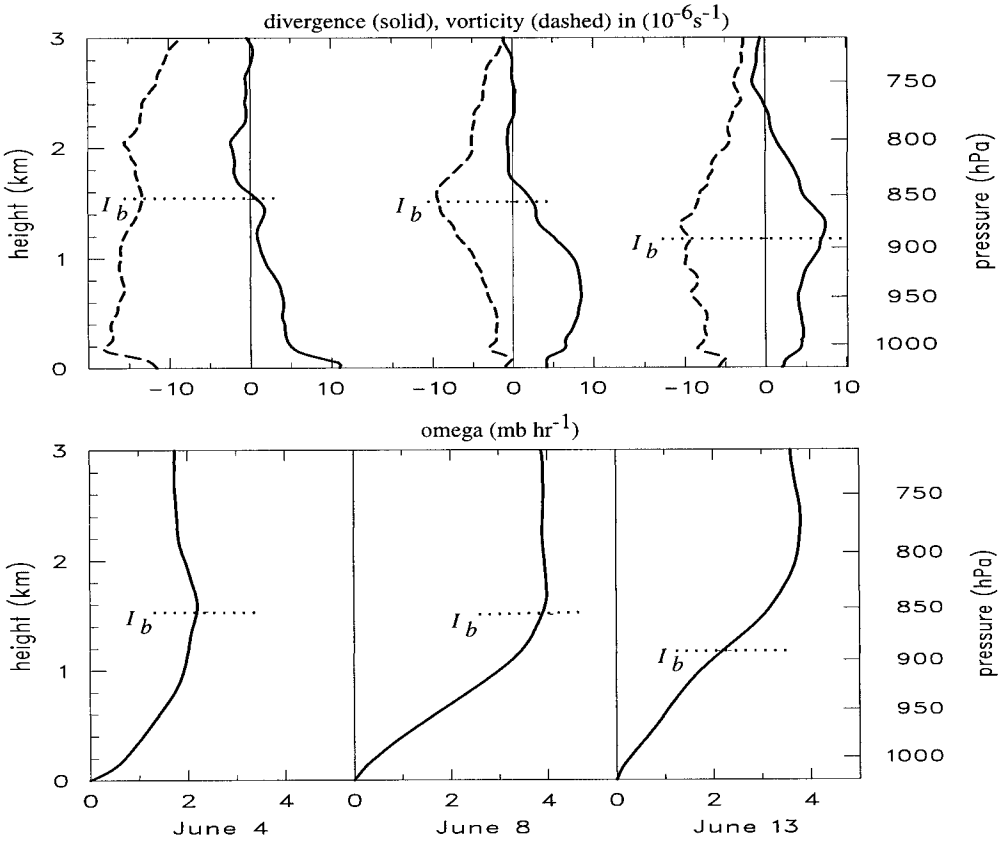

FIG. 14. Large-scale fields averaged over three 24-h periods: 4 June (leftmost curves), 8 June (middle curves), 13 June 1000 UTC to 14 June 0900 UTC (rightmost curves); divergence (solid) and relative vorticity (dashed) (top) and vertical motion (bottom). Daily averaged level of inversion base (I_b) is indicated with horizontal dotted line.

second cloud layer at this level, we look to the soundings at SM and *VL* (Fig. 16) for a possible explanation. Soundings at both these sites (but in particular SM) show moistening near 2 km, suggesting that a second inversion and cloud layer may have formed at this level and resulting in the secondary peaks of apparent moistening and cooling. Despite the large profile differences above 800 m, below this level all periods are characterized by a positive Q_1 and negative Q_2, suggesting a vertical convergence of eddy heat and moisture fluxes within this near-surface layer.

7. Concluding remarks

Rawinsonde data and model-generated radiative heating profiles have been used to investigate vertical distributions of the apparent heat source, apparent moisture sink, and convective fluxes from ASTEX for the period 1–15 June 1992. During this period the mean level of the inversion base was approximately 1460 m decreasing from near 1800 m on 1 June to under 1200 m on 15 June. Mean profiles for this period show a large apparent heat sink and apparent moisture source near the inversion base with peak cooling and moistening rates of -4 and -8 K day^{-1}, respectively. These features reflect the cooling and moistening effects of clouds that detrain near the inversion layer. While such distributions are representative of a 2-week mean over ASTEX, they are also observed, under certain conditions, in other regions with dramatically different vertical thermal structures. For example, similar profiles were diagnosed by NE74 for an undisturbed 5-day period in the trade wind regime during BOMEX, and over the Kurishio current (Nitta 1976) for a 3-day period of warm southerly advection during the Air Mass Transformation Experiment. Similar apparent heat sink and apparent moisture source distributions were found over the western Pacific warm pool during westerly wind bursts and suppressed, light wind periods in the Tropical Ocean Global Atmosphere Coupled Ocean–Atmosphere Response Experiment by Johnson and Lin (1997). They concluded that shallow cumulus play an important role in moistening the lower troposphere over the warm pool, either to prepare the atmosphere for future deep convection following a westerly wind burst, or to counterbalance the desiccating effect of subtropical dry intrusions.

While the rates of apparent moistening and cooling

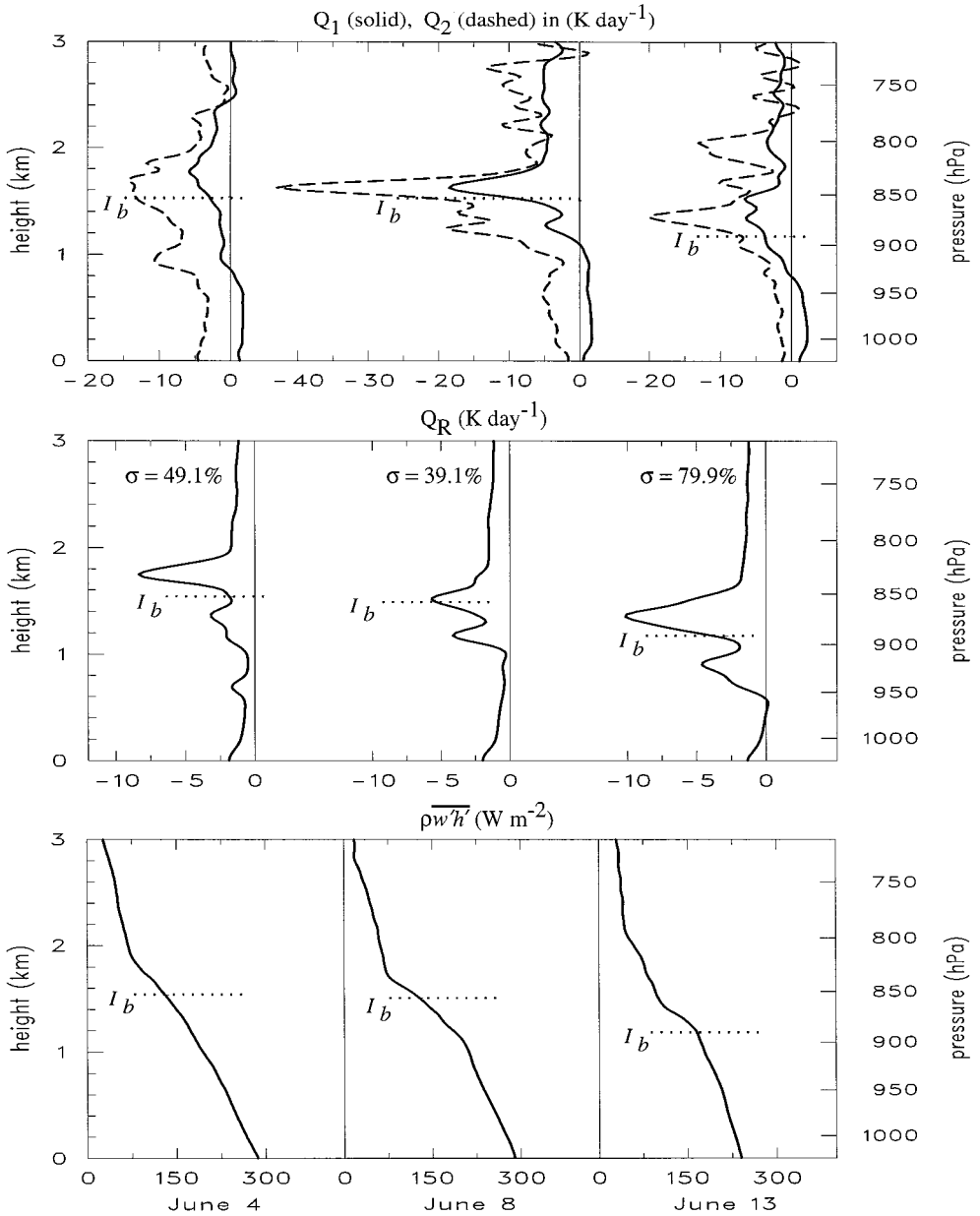

FIG. 15. Same as Fig. 14 except for (top) apparent heat source (solid) and apparent moisture sink (dashed), (middle) net radiative heating, and (bottom) vertical eddy flux of moist static energy. The 24-h average fractional cloudiness (σ) over the ASTEX triangle for each period is indicated in the middle panels.

vary somewhat among the studies cited above, their resemblance to each other results primarily from a trade wind–type stable layer that is strong enough to vertically limit the moistening effects of convection to the lower troposphere. Perhaps then these similarities in heat and moisture budgets between vastly different regions of our planet should not be surprising, in that the trade wind boundary layer with its associated capping inversion is a ubiquitous feature of the Tropics and subtropics.

The temporal variability of Q_1 and Q_2 profiles over ASTEX were strongly modulated on a synoptic timescale by the passage of fronts and fluctuations in the subsidence rate related to changes in the strength and position of the subtropical high. For example, on 8 June 1992 following the passage of a cold front through the ASTEX domain, the daily mean Q_1 and Q_2 rates increased to five times their 2-week mean values. Such events, which are linked to midlatitude disturbances, distinguish the ASTEX region from trade wind and tropical regimes, in that disturbances in these latter regions typically produce apparent drying and heating on deep tropospheric scales (Yanai et al. 1973; NE74). Conversely, convectively un-

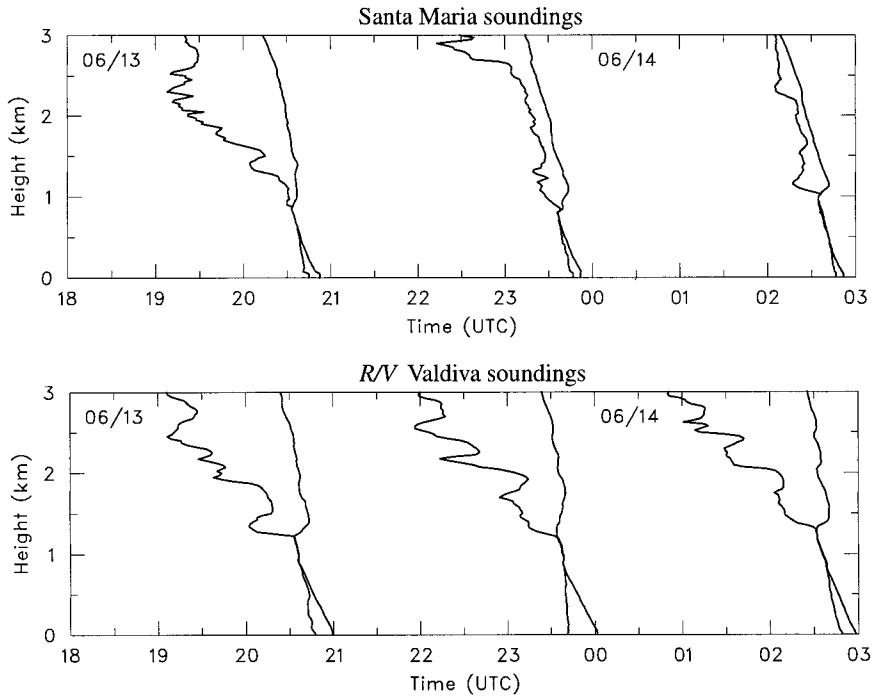

FIG. 16. Pairs of curves represent rawinsonde temperature (right) and dewpoint temperature (left) data for the period 13 June at 1800 UTC to 14 June at 0300 UTC (same period as in bottom panel of Fig. 9) for Santa Maria (top) and R/V *Valdivia* (bottom).

disturbed periods in the trades and Tropics tend to produce periods of low-level moistening.

During the 1–15 June period over the ASTEX triangle, fractional low cloudiness averaged 46% with a large synoptic variability in which cloud amount frequently changed by more that 20% on a timescale of a day or less. Relationships between changes in low cloud amount and fluctuations in large-scale budgets are often tenuous, considering that cloud maintenance involves complex feedbacks between radiation, microphysics, surface fluxes, and convection (Bretherton et al. 1995b). Nevertheless, from the ASTEX cloudiness time series we observed that the two largest increases in low cloud amount over this region occurred coincidentally with periods of reduced large-scale subsidence and were preceded by a period of enhanced convective fluxes that served to moisten the inversion layer.

Radiative divergence estimates were made for the ASTEX triangle using NCAR's community radiation model in conjunction with sounding data and a simple procedure to define cloud boundaries and liquid water content. The ASTEX mean Q_R profile shows cooling throughout the tropospheric column, maximizing in a 500 m deep layer centered near the mean inversion base at a rate of -3 K day^{-1}. This profile contrasts to the BOMEX mean Q_R, which has a slight minimum in cooling of -0.5 K day^{-1} centered near the inversion base. Presumably the Q_R profile differences between these regions are related to the higher fractional cloudiness over the ASTEX region. Comparison between computed surface radiative fluxes and buoy observations over the ASTEX region show excellent agreement.

Using budget computations of Q_1 and Q_2 along with model-generated profiles of Q_R, we analyzed the vertical eddy flux of moist static energy. The ASTEX mean profile of $\rho\overline{w'h'}$ decreases from its surface maximum of 125 W m^{-2} to about 10% of this value at 2 km. The magnitude of these fluxes is about 60% of that observed in BOMEX, presumably due to the lower SSTs in the ASTEX region (19.4° vs 28.1°C). Comparison of our computed surface fluxes to buoy observations for this period suggests that our estimates may be too large by about 20%. Finally, vertical eddy fluxes over ASTEX are strongly modulated on synoptic timescales, varying between zero and two times their mean value on a scale of a few days.

In closing, we note that this paper has focused on the mean structure and synoptic variability of large-scale fields and on the heat and moisture budgets over the ASTEX region. We have not used our diagnosed ASTEX profiles of $\rho\overline{w'h'}$ to compute convective mass fluxes and the thermodynamic properties within convective elements, as was done by Yanai et al. (1973) using a bulk cloud model and by Nitta (1975) using a spectral cloud model. This is an interesting problem that probably requires a cloud model more general than those used by Yanai et al. and Nitta because of the large fractional cloudiness in ASTEX. Another interesting problem, which is beyond the scope of this paper, concerns the use of mixing line diagrams (Betts and Al-

brecht 1987) to better understand the convective processes operating during combined cumulus–stratocumulus cloud regimes. Finally, in a forthcoming paper the diurnal variability of meteorological fields and convective and radiative fluxes in ASTEX will be compared to that in other regions such as BOMEX, in order to deepen our understanding of why regional phase and amplitude differences exist in the diurnal cycle.

Acknowledgments. We thank Chris Bretherton for his advice concerning the ECMWF data, Kelley Wittmeyer for making the ECMWF data accessible to us, John Davis and Mike Kelly for their help interpreting the radiative transfer computations, Shelby Frisch for providing the Porto Santo cloud radar data, Jim Kossin for computing the associated Legendre functions used in the appendix, and Stephan de Roode for his helpful suggestions. This research was supported by the Office of Naval Research under Grant N00014-91-J-1422.

APPENDIX

Assessment of Sampling and Interpolation Errors on the Divergence Calculation

Because of the large distances between the vertices of the ASTEX triangle, the accuracy of the divergence calculation may be compromised by inadequate sampling and interpolation of the horizontal wind field. To evaluate the magnitude of this error, we have used the line integral method described in (1) to compute the divergence, over the ASTEX triangle, of a flow field that (in a continuous sense) has no divergence. To accomplish this we have specified the winds at the vertices of the ASTEX triangle to be those associated with a nondivergent barotropic Rossby–Haurwitz wave. The nondivergent flow associated with this wave is described by the streamfunction $\psi(\lambda, \mu, t) = \Psi Y_n^m(\lambda, \mu)e^{i\nu_n^m t}$, where $Y_n^m(\lambda, \mu) = P_n^m(\mu)e^{im\lambda}$ is the spherical harmonic, $P_n^m(\mu)$ the associated Legendre function, λ the longitude, $\mu = \sin\phi$ the sine of the latitude, Ψ a constant, m the zonal wavenumber, n the total wavenumber, $\nu_n^m = 2\Omega m/[n(n + 1)]$ the Rossby–Haurwitz wave frequency, and Ω the earth's rotation rate. The velocity components in the eastward and northward directions are given in terms of ψ by $u = -\partial\psi/a\partial\phi$ and $v = \partial\psi/a\cos\phi\partial\lambda$, where a is the radius of the earth.

We now consider the accuracy of the divergence calculation as related to the horizontal scale of the Rossby–Haurwitz waves. Since the spherical harmonic satisfies $\nabla^2 Y_n^m = -a^{-2}n(n + 1)Y_n^m$, the factor $n(n + 1)/a^2$ can be interpreted as the sum of the squares of the two horizontal wavenumbers (i.e., $k^2 + l^2$, where k and l are dimensional Cartesian wavenumbers). Thus, for modes with an aspect ratio of unity ($k = l$), we have $2k^2 = n(n + 1)/a^2$. This can be written as $L_n = \{2\pi^2a^2/[n(n + 1)]\}^{1/2}$, where $L_n = \pi/k$ is the half-wavelength of mode n. Defining a characteristic length scale of the ASTEX triangle as $L_\triangle$ = (area of ASTEX triangle)$^{1/2}$, we pose the following question. What is the value of n at which $L_n = L_\triangle$? In other words, what is minimum wavelength that can be resolved by the ASTEX triangle? Since the area of the ASTEX triangle is 3.86×10^{11} m^2, we find that $n = 45$. This suggests that we should expect significant divergence errors for Rossby–Haurwitz wave patterns with $n \geq 45$. Significant divergence errors can also occur at smaller n if the Rossby–Haurwitz wave amplitude $|\Psi|$ is large. For example, for synoptic-scale Rossby–Haurwitz waves with $m = 6$ and $n = 6, 7, 8, 9$, and with Ψ chosen such that the average wind speed at the vertices of the ASTEX triangle is 7 m s^{-1}, the mean magnitude of the calculated line integral divergences averaged over the passage of these four waves is 0.79×10^{-6} s^{-1}. This divergence error, which varies substantially from one wave to the next, depends significantly on where a wave's nodal crossings occur relative to the ASTEX triangle. This value of 0.79×10^{-6} s^{-1} should be compared with the mean ASTEX divergence profile shown in Fig. 7a, which indicates a boundary layer value of 4.0×10^{-6} s^{-1}. While the spectra and type of waves that occurred over the ASTEX triangle during 1–15 June 1992 are complex, this analysis suggests that our divergence calculation could be in error by 20% due to inadequate sampling and interpolation of the horizontal wind field.

REFERENCES

Albrecht, B. A., C. S. Bretherton, D. Johnson, W. H. Schubert, and A. S. Frisch, 1995: The Atlantic Stratocumulus Transition Experiment (ASTEX). *Bull. Amer. Meteor. Soc.*, **76,** 889–903.

Augstein, E., H. Riehl, F. Ostapoff, and V. Wagner, 1973: Mass and energy transports in an undisturbed Atlantic trade-wind flow. *Mon. Wea. Rev.*, **101,** 101–111.

——, H. Schmidt, and F. Ostapoff, 1974: The vertical structure of the atmospheric planetary boundary layer in undisturbed trade winds over the Atlantic Ocean. *Bound.-Layer Meteor.*, **6,** 129–150.

Bellec, B., A. Brisson, P. Le Borgne, and A. Marsouin, 1992: Operational cloud classification with METEOSTAT data. *Proc. Central Symp. Int. Space Year Conf.*, ESA SP-341, Munich, Germany, European Space Agency, 283–288.

Betts, A. K., 1975: Parametric interpretation of trade-wind cumulus budget studies. *J. Atmos. Sci.*, **32,** 1934–1945.

——, and B. A. Albrecht, 1987: Conserved variable analysis of the convective boundary layer thermodynamic structure over the tropical oceans. *J. Atmos. Sci.*, **44,** 83–99.

Bluth, R. T., and B. A. Albrecht, 1993: Atlantic Stratocumulus Transition Experiment and Marine Aerosol and Gas Exchange June 1992 experiment summary. Part I—Mission summaries. Department of Meteorology, The Pennsylvania State University, Tech. Report, 285 pp. [Available from Department of Meteorology, The Pennsylvania State University, University Park, PA 16802.]

Bretherton, C. S., 1992: A conceptual model of the stratocumulus-trade-cumulus transition in the subtropical oceans. *Proc. 11th Int. Conf. on Clouds and Precipitation*, Vol. 1, Montreal, PQ, Canada, International Commission on Clouds and Precipitation and International Association of Meteorology and Atmospheric Physics, 374–377.

——, P. Austin, and S. T. Siems, 1995a: Cloudiness and marine boundary layer dynamics in the ASTEX Lagrangian experi-

ments. Part II: Cloudiness, drizzle, surface fluxes, and entrainment. *J. Atmos. Sci.,* **52,** 2724–2735.

——, E. Klinker, A. K. Betts, and J. A. Coakley Jr., 1995b: Comparison of ceilometer, satellite, and synoptic measurements of boundary layer cloudiness and the ECMWF diagnostic cloud parameterization scheme during ASTEX. *J. Atmos. Sci.,* **52,** 2736–2751.

Brink, N. J., K. A. Moyer, R. P. Trask, and R. A. Weller, 1995: The Subduction Experiment: Mooring field program and data summary. Tech. Rep. WHOI-95-08, 113 pp. [Available from WHOI, Woods Hole, MA 02543.]

Cahalan, R. F., and D. Silberstein, 1995: Liquid water path and plane parallel albedo bias during ASTEX. *J. Atmos. Sci.,* **52,** 3002–3012.

Cox, S. K., 1973: Radiation components of the energy budget for BOMEX. Atmospheric Science Paper 208, Colorado State University, Fort Collins, CO, 43 pp. [Available from Department of Atmospheric Science, Colorado State University, Fort Collins, CO 80523.]

Delnore, V. L., 1972: Diurnal variation of temperature and energy budget for the oceanic mixed layer during BOMEX. *J. Phys. Oceanogr.,* **2,** 239–247.

de Roode, S. R., and P. G. Duynkerke, 1996: Dynamics of cumulus rising into stratocumulus as observed during the first ''Lagrangian'' experiment of ASTEX. *Quart. J. Roy. Meteor. Soc.,* **122,** 1597–1623.

——, and P. G. Duynkerke, 1997: Observed Lagrangian transition of stratocumulus into cumulus during ASTEX: Mean state and turbulence structure. *J. Atmos. Sci.,* **54,** 2157–2173.

Dorman, C. E., and R. H. Bourke, 1981: Precipitation over the Atlantic Ocean, 30°S to 70°N. *Mon. Wea. Rev.,* **109,** 554–563.

Duynkerke, P. G., H. Zhang, and P. J. Jonker, 1995: Microphysical and turbulent structure of nocturnal stratocumulus as observed during ASTEX. *J. Atmos. Sci.,* **52,** 2763–2777.

Gutnick, M., 1958: Climatology of the trade-wind inversion in the Caribbean. *Bull. Amer. Meteor. Soc.,* **39,** 410–420.

Hartmann, D. L., M. E. Ockert-Bell, and M. L. Michelsen, 1992: The effect of cloud type on earth's energy balance: Global analysis. *J. Climate,* **5,** 1281–1304.

Hogg, D. C., F. O. Guiraud, J. B. Snider, M. T. Decker, and E. R. Westwater, 1983: A steerable dual-channel microwave radiometer for measurement of water vapor and liquid in the troposphere. *J. Climate Appl. Meteor.,* **22,** 789–806.

Holland, J. Z., and E. M. Rasmusson, 1973: Measurements of the atmospheric mass, energy, and momentum budgets over a 500-kilometer square of tropical ocean. *Mon. Wea. Rev.,* **101,** 44–55.

Johnson, R. H., and X. Lin, 1997: Episodic trade wind regimes over the western Pacific warm pool. *J. Atmos. Sci.,* **54,** 2020–2034.

Kiehl, J. T., J. J. Hack, and B. P. Briegleb, 1994: The simulated earth radiation budget of the National Center of Atmospheric Research community climate model CCM2 and comparisons with the Earth Radiation Budget Experiment (ERBE). *J. Geophys. Res.,* **99,** 20 815–20 827.

Klein, S. A., and D. L. Hartmann, 1993: The seasonal cycle of low stratiform clouds. *J. Climate,* **6,** 1587–1606.

Klett, J. D., 1981: Stable analytical inversion solution for processing lidar returns. *Appl. Opt.,* **20,** 211–221.

——, 1986: Extinction boundary value algorithms for lidar inversion. *Appl. Opt.,* **25,** 2462–2464.

Lilly, D. K., 1968: Models of cloud-topped mixed layers under a strong inversion. *Quart. J. Roy. Meteor. Soc.,* **94,** 292–309.

Martner, B. E., and R. A. Kropfli, 1993: Observations of multi-layered clouds using K_a-band radar. FIRE Cirrus Results, 1993. NASA Conference Pub. 3238, 175 pp. [Available from Environmental Technology Laboratory, 325 Broadway, Boulder, CO 80303.]

McClatchey, R. A., R. W. Fenn, E. J. A. Selby, E. E. Volz, and J. S. Garing, 1971: Optical properties of the atmosphere (revised). AFCRL Environmental Research Paper 354, Bedford, MA, 85 pp. [Available from Air Force Cambridge Research Laboratory, Bedford, MA 01730.]

Miller, M. A., and B. A. Albrecht, 1995: Surface-based observations of mesoscale cumulus–stratocumulus interaction during ASTEX. *J. Atmos. Sci.,* **52,** 2809–2826.

Molinari, J., and S. Skubis, 1988: Calculation of consistent flux and advective terms from adjusted vertical profiles of divergence. *Mon. Wea. Rev.,* **116,** 1829–1837.

Moyer, K. A., and R. A. Weller, 1997: Observations of surface forcing from the Subduction Experiment: A comparison with global model products and climatological datasets. *J. Climate,* **10,** 2725–2742.

Nitta, T., 1975: Observational determination of cloud mass flux distributions. *J. Atmos. Sci.,* **32,** 73–91.

——, 1976: Large-scale heat and moisture budgets during the Air Mass Transformation Experiment. *J. Meteor. Soc. Japan,* **54,** 1–14.

——, and S. Esbensen, 1974: Heat and moisture budget analyses using BOMEX data. *Mon. Wea. Rev.,* **102,** 17–28.

Pond, S., G. T. Phelps, J. E. Paquin, G. McBean, and R. W. Stewart, 1971: Measurements of turbulent fluxes of momentum, moisture and sensible heat over the ocean. *J. Atmos. Sci.,* **28,** 901–917.

Randall, D. A., J. A. Coakley, C. W. Fairall, R. A. Kropfli, and D. H. Lenschow, 1984: Outlook for research on marine subtropical stratocumulus clouds. *Bull. Amer. Meteor. Soc.,* **65,** 1290–1301.

——, J. A. Abeles, and T. G. Corsetti, 1985: Seasonal simulation of the planetary boundary layer and boundary layer stratocumulus clouds with a general circulation model. *J. Atmos. Sci.,* **42,** 641–675.

——, B. A. Albrecht, S. K. Cox, D. W. Johnson, P. Minnis, W. B. Rossow, and D. O'C. Starr, 1996: On FIRE at ten. *Advances in Geophysics,* Vol. 38, Academic Press, 37–177.

Riehl, H., C. Yeh, J. S. Malkus, and N. E. La Seur, 1951: The Northeast trades of the Pacific Ocean. *Quart. J. Roy. Meteor. Soc.,* **77,** 598–626.

Schubert, W. H., P. E. Ciesielski, C. Lu, and R. H. Johnson, 1995: Dynamical adjustment of the trade wind inversion layer. *J. Atmos. Sci.,* **52,** 2941–2952.

Sellers, W. D., 1965: *Physical Climatology.* University of Chicago Press, 272 pp.

Séze, G., and M. Desbois, 1987: Cloud cover analysis from satellite imagery using spatial and temporal characteristics of the data. *J. Climate Appl. Meteor.,* **26,** 219–249.

Stevens, E. L., 1994: Comparison of sounding, profiler, radar and ceilometer data from Porto Santo Island during ASTEX. Atmospheric Science Paper 551, Colorado State University, Fort Collins, CO, 72 pp. [Available from Department of Atmospheric Science, Colorado State University, Fort Collins, CO 80523.]

von Ficker, H., 1936: Die passatinversion. *Veröf. Meteor. Inst. Univ. Berlin,* **1,** (4), 1–33.

Wang, Q., and D. H. Lenschow, 1995: An observational study of the role of penetrating cumulus in a marine stratocumulus-topped boundary layer. *J. Atmos. Sci.,* **52,** 2778–2787.

Weller, R. A., D. L. Rudnick, R. E. Payne, J. P. Dean, N. J. Pennington, and R. P. Trask, 1990: Measuring near-surface meteorology over the ocean from an array of surface moorings in the subtropical convergence zone. *J. Atmos. Oceanic. Technol.,* **7,** 85–103.

White, A. B., C. W. Fairall, and J. B. Snider, 1995: Surface-based remote sensing of marine boundary layer cloud properties. *J. Atmos. Sci.,* **52,** 2827–2838.

Wyant, M. C., C. S. Bretherton, H. A. Rand, and D. E. Stevens, 1997: Numerical simulations and a conceptual model of the subtropical marine stratocumulus to trade cumulus transition. *J. Atmos. Sci.,* **54,** 168–192.

Yanai, M., S. Esbensen, and J.-H. Chu, 1973: Determination of bulk properties of tropical cloud clusters from large-scale heat and moisture budgets. *J. Atmos. Sci.,* **30,** 611–627.